

Nucleation, Growth, and Kinetic Roughening of Metal(100) Homoepitaxial Thin Films[†]

J. W. Evans^{*,‡} and M. C. Bartelt[§]

Department of Mathematics, IPRT, and Ames Laboratory, Iowa State University,
Ames, Iowa 50011

Received September 1, 1994. In Final Form: September 5, 1995[®]

A unified analysis is presented of submonolayer nucleation and growth of two-dimensional islands and the subsequent transition to multilayer growth during metal-on-unreconstructed metal(100) homoepitaxy. First, we review and augment recent developments in submonolayer nucleation theory for general critical size i (above which islands are effectively stable against dissociation). We discuss choices of “capture numbers” for aggregation of adatoms with islands, and ramifications for island density scaling with deposition flux and substrate temperature. We also characterize a “direct” transition from critical size $i = 1$ to a well-defined regime of $i = 3$ scaling, with increasing temperature, for sufficiently strong adatom–adatom bonding. We note that there exists no well-defined regime of integer $i > 3$. The submonolayer island distribution provides a template for subsequent unstable multilayer growth or “mounding” (which we contrast with “self-affine” growth). This mounding is induced by the presence of a step-edge barrier for downward diffusive transport in these systems. We characterize resulting oscillatory height correlation functions and non-Gaussian height and height-difference distributions. We also develop an appropriate kinematic diffraction theory to elucidate the oscillatory decay of Bragg intensities and the evolution from split to nonsplit diffraction profiles. Finally, we analyze experimental data for Fe(100) and Cu(100) homoepitaxy and extract key activation barriers for these systems.

I. Introduction

In this report we review and further develop understanding of submonolayer nucleation and growth of two-dimensional (2D) islands during deposition,^{1–3} and of the subsequent kinetic roughening of the growing multilayer film.^{4,5} We focus on application to metal-on-unreconstructed metal(100) homoepitaxy.³ Deposition for typical fluxes and substrate temperatures results in the system being driven far from equilibrium, since equilibrating processes such as coarsening (e.g., via Ostwald ripening⁶ or large cluster diffusion⁷) are ineffective on the time scale of deposition. The film structure is thus kinetically rather than thermodynamically determined. Through modeling, one attempts to elucidate the detailed atomic mechanisms controlling film structure, while extracting basic system parameters.

These parameters include the activation barrier, E_d , for terrace diffusion, the adatom–adatom bond energy, E_{bond} , and the additional Ehrlich–Schwoebel or step-edge barrier, E_{Sch} , to downward diffusive transport.⁸ At lower

temperatures, T , where island formation is irreversible, the submonolayer island density, N_{av} , is controlled by the rate for the dominant terrace diffusion mechanism, $h = \nu \exp[-E_d/(k_B T)]$, be it bridge hopping or place exchange.⁹ However, N_{av} also depends on E_{bond} at higher T where the effective rate at which single bonds break, $h_{\text{diss}} = \nu \exp[-(E_d + E_{\text{bond}})/(k_B T)]$, is significant and thus where island dissociation is operative. The kinetic roughening of multilayer films is very sensitive to the dominant rate, $h_{\text{Sch}} = \nu \exp[-(E_d + E_{\text{Sch}})/(k_B T)]$, at which adatoms are transported down off the edge of islands, be it by hopping or exchange. Here we have assumed a single value for the prefactors, ν , and ignore the possibility of distinct step-edge barriers at kinks.

A general theme in this paper is that submonolayer structure, which is determined by the details of the nucleation and growth processes, influences the subsequent structure of the growing multilayer film. This correlation should be particularly strong for thin films up to a few dozen monolayers, which is often the regime of experimental interest. Thus below we first describe models for submonolayer nucleation and growth of islands, before discussing general paradigms and specific models for multilayer kinetic roughening. We focus on recent developments and controversies.

The following models for submonolayer nucleation and growth have been studied by simulation and rate equations. In all cases, atoms deposit randomly at rate R per site, diffuse on the terrace with rate h , and subsequently nucleate, aggregate with, and possibly dissociate from islands.

(A) Models with Prescribed Critical Size, i . Here islands or clusters of size $s > i$ are stable and never dissociate.^{1–3} For $i > 1$, key parameters controlling nucleation of stable islands include E_d and the binding energy, $E_i > 0$, for critical clusters of i adatoms. (E_i is related to E_{bond} .) In rate-equation studies, it is often

[†] Presented at the symposium on Advances in the Measurement and Modeling of Surface Phenomena, San Luis, Argentina, August 1994.

[‡] Department of Mathematics.

[§] IPRT.

[®] Abstract published in *Advance ACS Abstracts*, January 1, 1996.

(1) Venables, J. A. *Philos. Mag.* **1973**, *27*, 697.

(2) Stoyanov, S.; Kashchiev, K. *Curr. Top. Mater. Sci.* **1981**, *7*, 69.

(3) Evans, J. W.; Bartelt, M. C. *J. Vac. Sci. Technol., A* **1994**, *12*, 1800.

(4) See, e.g., *Kinetics of Ordering and Growth at Surfaces*; Lagally, M. G., Ed.; Plenum: New York, 1990.

(5) Yang, H.-N.; Lu, T.-M.; Wang, G.-C. *Phys. Rev. Lett.* **1992**, *68*, 2612. Yang, H.-N.; Wang, G.-C.; Lu, T.-M. *Diffraction from Rough Surfaces and Dynamic Growth Fronts*; World Scientific, Singapore, 1993; *Phys. Rev. B* **1995**, *51*, 17932.

(6) Ernst, H.-J.; Fabre, F.; Lapujoulade, J. *Phys. Rev. Lett.* **1992**, *69*, 458.

(7) Wen, J.-M.; Evans, J. W.; Bartelt, M. C.; Burnett, J. W.; Thiel, P. A. *Phys. Rev. Lett.*, in press. Wen, J.-M.; Chang, S.-L.; Burnett, J. W.; Evans, J. W.; Thiel, P. A. *Phys. Rev. Lett.* **1994**, *73*, 2591. *Evolution of Thin-Film and Surface Structure and Morphology*; Demczyk, B. G.; Williams, E. D.; Garfunkel, E.; Clemens, B. M.; Cuomo, J. E. MRS Proceedings; Materials Research Society: Pittsburgh, PA, 1995; Vol. 355, p 15.

(8) Schwoebel, R. J. *J. Appl. Phys.* **1969**, *40*, 614.

(9) Feibelman, P. J. *Phys. Rev. Lett.* **1990**, *65*, 729; *Surf. Sci.* **1994**, *299/300*, 426.

assumed that substable clusters are in quasiequilibrium.¹⁰ In simulation studies, one must prescribe the dissociation and recombination of substable islands, stable-island structure, mobility, and possible restructuring before and after coalescence with other islands,¹¹ etc.

(B) Models with Prescribed Bond Scission.¹² Choices include (i) no breaking of any (single or multiple) bonds, corresponding to $i = 1$; or (ii) breaking of single, but not multiple bonds. The latter produces a model similar to $i = 2$ on a triangular lattice (triangular trimers are stable, but not larger islands with singly bonded adatoms) and $i = 3$ on a square lattice (tetramers are stable, but not larger islands with singly bonded atoms). Island restructuring must also be prescribed. These models produce behavior similar to (A).

(C) Nearest-Neighbor (NN) Pair-Interaction Models.^{13–15} Here there is no *a priori* prescription of island stability and structure, or of the critical size, i . Adatoms can hop to empty nearest neighbor sites, with an activation barrier commonly chosen to satisfy $E_{\text{act}} = E_d + nE_{\text{bond}}$, where n is the number of intralayer NN adatoms before hopping, and again $E_{\text{bond}} > 0$ is the bond energy. Here hopping at island edges and around island corners is greatly inhibited, contrasting behavior in metal-(100) homoepitaxy.³ Thus equilibration of island shapes to compact (square) forms, via edge diffusion, is difficult. (However, evaporation–recondensation can provide an efficient alternative pathway¹⁵ for higher T .) Of course, one could implement alternative forms of E_{act} which enhance rates for edge hops, while preserving detailed balance.¹⁶

(D) Classically “Exact” Treatments of Surface Diffusion. At the level of transition state theory, this requires a “catalogue” of exact E_{act} values¹⁷ for all configurations of the local environment influencing adatom hop rates. These are incorporated into growth simulations. Only approximate E_{act} values can be obtained from theories such as the embedded atom method¹⁸ (EAM), corrected effective medium theory¹⁹ (CEM) and its simplifications, or effective medium theory²⁰ (EMT). Since nucleation behavior depends sensitively on the values of a few key barriers, uncertainties in these values limit the predictive capability of this approach. However, some success has been achieved²¹ by, e.g., uniformly rescaling all theoretical values to match an observed E_d .

A central issue of nucleation theory is the scaling of N_{av} with substrate temperature, T , and deposition flux, R . Traditional rate-equation analysis for models of type (A) yields^{1–3}

$$N_{\text{av}} \sim (R/\nu)^{\chi} \exp[E/(k_B T)] \quad (1)$$

with

$$\chi = i/(i + 2) \text{ and } E = \chi(E_d + E_i/\hbar)$$

at fixed coverage, θ , and assuming quasi-equilibrium of substable clusters. However, the traditional analysis assumes that the “capture numbers”, K_s , describing the propensity of islands to incorporate diffusing adatoms, are independent of island size, s . In section II, we discuss a recent and more realistic treatment for $i = 1$, and generalizations to $i > 1$, but only considering the traditional models of type A. A recent simulation study^{14,15} using a model of type C suggested that the classic scaling (1) breaks down, and that there are no well-defined critical sizes with integer valued $i > 1$. If true, this would have significant ramifications for the interpretation of experimental data. Thus we address and clarify this issue in section III. We shall always assume that stable islands are immobile. It has been shown^{22–24} that small cluster mobility can potentially affect N_{av} scaling, but we have not found²⁴ strong experimental evidence that small cluster mobility is significant in metal(100) homoepitaxy at low T . (At higher T , the increase in critical size, i , has the dominant effect on N_{av} .) However, we note that the island size distribution is much more sensitive to even small amounts of small cluster mobility (see section VI and ref 24).

For multilayer growth and kinetic roughening, two general paradigms, A and B below, are available to describe film morphology and evolution.^{25–28} Their common feature is that the film roughens globally due to noise in the deposition process but that counterbalancing local equilibrating processes tend to produce a locally stationary structure. The interface width, W , defined as the standard deviation of the film height distribution, characterizes surface roughness. It is assumed²⁵ to have the asymptotic form $W \sim \theta^{\beta}$ (or $W^2 \sim \ln \theta$, if $\beta = 0$), for multilayer films with coverages (or average heights) $\theta \gg 1$.

(A) Selection of a Locally Self-Affine Stationary Structure.²⁵ Here the local structure of the film becomes invariant under a rescaling of the lateral dimensions by $\mathbf{x} \rightarrow \lambda \mathbf{x}$, and of the vertical dimension by $z \rightarrow \lambda^{\alpha} z$. The exponent α is nontrivial and, together with β mentioned above, determines the universality class of film growth. A large number of so-called MBE models,²⁹ which display this behavior, have been developed to describe real film growth processes and to determine associated universality. However, these typically oversimplify or neglect the process of submonolayer nucleation and growth of islands, neglect the step-edge barrier, and have focused on scaling in the asymptotic regime of very thick films.

(B) Unstable Growth or “Mounding” Induced by a Step-Edge Barrier.^{26–28} Here the tendency for adatoms to be reflected at descending steps leads to biased incorporation at ascending steps. This constitutes a

(10) Walton, D. J. *Chem. Phys.* **1962**, *37*, 2182.

(11) Bartelt, M. C.; Evans, J. W. *Surf. Sci.* **1993**, *298*, 421. *Common Themes and Mechanisms of Epitaxial Growth*; Fuoss, P., Tsao, J., Kisker, D., Zangwill, A., Kuech, T. *MRS Proceedings* Materials Research Society: Pittsburgh, PA, 1993; Vol. 312, p 255.

(12) Amar, J. G.; Family, F. *Phys. Rev. Lett.* **1995**, *74*, 2066. *Fractal Aspects of Materials* Family, F., Meakin, P., Sapoval, B., Wool, R. *MRS Proceedings* Materials Research Society: Pittsburgh, PA, 1995; Vol. 367. Family, F.; Amar, J. G. *Mater. Sci. Eng. B* **1995**, *30*, 149.

(13) Clarke, S.; Vvedensky, D. D. *J. Appl. Phys.* **1988**, *63*, 2272.

(14) Ratsch, C.; Zangwill, A.; Šmilauer, P.; Vvedensky, D. D. *Phys. Rev. Lett.* **1994**, *72*, 3194.

(15) Ratsch, C.; Šmilauer, P.; Zangwill, A.; Vvedensky, D. D. *Surf. Sci.* **1995**, *329*, L599.

(16) Bartelt, M. C.; Perkins, L. S.; Evans, J. W. *Surf. Sci.* **1995**, *344*, L1193.

(17) Voter, A. *SPIE* **1987**, *821*, 214. Barkema, G. T.; Biham, O.; Breeman, M.; Boerma, D. O.; Vidali, G. *Surf. Sci.* **1994**, *306*, L569.

(18) Daw, M. S.; Baskes, M. I. *Phys. Rev. Lett.* **1983**, *50*, 1285; *Phys. Rev. B* **1984**, *29*, 6443.

(19) Raeker, T. J.; DePristo, A. E. *Int. Rev. Phys. Chem.* **1991**, *10*, 1. Perkins, L. S.; DePristo, A. E. *Surf. Sci.* **1995**, *325*, 169.

(20) Nørskov, J. K.; Lang, N. D. *Phys. Rev. B* **1980**, *21*, 2131.

(21) Jacobsen, J.; Jacobsen, K. W.; Stoltze, P.; Nørskov, J. *Phys. Rev. Lett.* **1995**, *74*, 2295.

(22) Villain, J.; Pimpinelli, A.; Tang, L.; Wolf, D. J. *Phys. I* **1992**, *2*, 2107. Villain, J.; Pimpinelli, A.; Wolf, D. *Comments Cond. Mater. Phys.* **1992**, *16*, 1.

(23) Liu, S.; Böni, L.; Metiu, H. *Phys. Rev. B* **1995**, *52*, 2907.

(24) Bartelt, M. C.; Günther, S.; Kopatzki, E.; Behm, R. J.; Evans, J. W. *Phys. Rev. B*, in press.

(25) *Dynamics of Fractal Surfaces*; Family, F., Vicsek, T., Eds.; World Scientific: Singapore, 1991.

(26) Johnson, M. D.; Orme, C.; Hunt, A. W.; Graff, D.; Sudijono, J.; Sander, L. M.; Orr, B. G. *Phys. Rev. Lett.* **1994**, *72*, 116.

(27) Siegert, M.; Plischke, M. *Phys. Rev. Lett.* **1994**, *73*, 1517.

(28) Elkinani, I.; Villain, J. *J. Phys. I* **1994**, *4*, 949.

(29) Wolf, D. E.; Villain, J. *Europhys. Lett.* **1990**, *13*, 389. Das Sarma, S.; Tamborenea, P. *Phys. Rev. Lett.* **1991**, *66*, 325. Lai, Z.-W.; Das Sarma, S. *Phys. Rev. Lett.* **1991**, *66*, 2348.

lateral mass flow or current in the *uphill* direction. This current produces unstable growth, and specifically “mounding”. One possibility is that due to the presence of some counterbalancing *downhill* current, a stable slope of the mounds is selected, and thereafter the mounds continue to coarsen with both base width and their height increasing as θ^n (so $\beta = n$ here). While the presence of a downhill current has been proposed based on crystal symmetry arguments,²⁷ it is primarily determined by details of the deposition dynamics, as we discuss below. We also note that recent simulation studies do not always find perfect slope selection and instead sometimes find a slowly increasing slope.³⁰

We describe basic real-space behavior in both these models in section IV, as well as the corresponding kinematic diffraction theory necessary for interpretation of surface-sensitive diffraction data in section V. While the self-affine models have received the most attention,²⁵ and the diffraction theory has been developed exclusively for these,⁵ the unstable growth models are more appropriate for the systems of interest here. For unstable growth models, we make some basic new observations concerning oscillatory height correlations, vertical asymmetry in the film height distribution, and deviations from anticipated Gaussian height-difference distributions, which lead to dramatic refinements in the existing diffraction theory.³¹

Next we remark that it is crucial to incorporate a correct description of adsorption site geometry, and a realistic treatment of the deposition dynamics, for precise modeling of multilayer growth in systems such as metal(100) homoepitaxy.³² An unphysical simple-cubic geometry with on-top adsorption sites has been used almost universally in previous modeling. In contrast, a 4-fold-hollow (4FH) adsorption site geometry applies for both fcc(100) and bcc(100) homoepitaxy, and the deposition dynamics involves a *downward funneling* or *deflection* from individual atoms, step edges, or other small microprotrusions to such 4FH sites.³² Other (nonthermal) transient mobility, clumping, and knockout processes are also possible during deposition and would affect film morphology.³²

Perhaps the most dramatic effect of incorporating realistic adsorption site geometry and dynamics is that one finds very smooth (rather than very rough) growth^{33,34} at low T . One might expect that these effects would quickly become insignificant with increasing T , i.e., with increasing diffusion length and submonolayer island sizes. However, replacing the standard simple-cubic geometry with a realistic geometry and deposition dynamics in standard MBE models produces significant differences in roughening behavior even for substantial diffusion lengths.³⁵ We shall also see that appropriate geometry and deposition dynamics are crucial ingredients in realistic models of unstable growth and mounding in metal(100) homoepitaxy.

Finally, in section VI, we apply the above ideas for submonolayer nucleation and growth, as well as multilayer kinetic roughening, to analyze in detail the experimentally observed behavior in Fe(100) and Cu(100) homoepitaxy.

II. Submonolayer Nucleation and Growth with Prescribed Critical Size

We first discuss “mean-field” rate-equation descriptions for nucleation and growth of *compact islands* with *isotropic diffusion* and *prescribed critical size* i , models of type A in section I. Here “mean-field” means that the local environment of each island is assumed to be independent of the size and shape of the island. We also assume that stable islands are immobile. Such rate equations have been invaluable in elucidating scaling behavior of the island density,^{1–3} N_{av} , although here we also note their limitations in predicting full island size distributions. Below, R denotes the deposition rate and h the isolated adatom diffusion rate, as described in section I.

Let N_s denote the density (per adsorption site) of islands of size s , so $\theta = \sum_{s \geq 1} s N_s$ is the total coverage, and $N_{av} = \sum_{s \geq i} N_s$. We also define $N_1^* = N_1/(1 - \theta)$ as the *renormalized* density of isolated adatoms on the bare substrate.¹ Then, for precoalescence θ , the rate equations for the densities of *stable* islands are^{1–3,14}

$$\begin{aligned} dN_{s>i}/dt = & R[(s-1)N_{s-1} - sN_s] \text{ on-top deposition} \\ & + R[b_{s-1}N_{s-1} - b_sN_s] \text{ adjacent deposition} \\ & + hN_1^*[K_{s-1}N_{s-1} - K_sN_s] \text{ aggregation} \quad (2) \end{aligned}$$

where $b_s \sim s^{1/2}$ gives the mean perimeter length for compact islands of size s atoms, and the K_s are “capture numbers” describing the propensity for islands of size s to capture diffusing adatoms. One typically assumes that islands of size $s \leq i$ are in quasi-equilibrium. This leads to the Walton relation^{1–3,10} for the density of critical clusters, $N_i \approx (1 - \theta) \exp[E_i/(k_B T)](N_1^*)^i$, which, together with the identity $\theta = Rt \approx N_1 + \sum_{s>i} s N_s$, allows integration of (2).

The solutions of (2) are expected to exhibit scaling of the form^{3,11}

$$N_{s>i} = [\theta/(s_{av})^2] F(s/s_{av}, \theta) \quad (3)$$

for large average island size, $s_{av} \equiv \sum_{s>i} s N_s / \sum_{s>i} N_s \sim \theta/N_{av}$. The scaling function, $F()$, satisfies $\int_0^\infty dx F(x, \theta) = \int_0^\infty dx x F(x, \theta) = 1$. The dependence of $F(x, \theta)$ on θ is weak in the precoalescence regime below about 0.2 monolayer (ML), but it is strong for higher coverages where significant island coalescence and, ultimately, percolation occur.¹¹ Since some degree of coalescence occurs even at low θ , there can be no strict “dynamic scaling”,³⁶ i.e., strict independence of θ (except for idealized “point island” models³⁷).

The scaling of N_{av} (or s_{av}) is most easily assessed by reducing the full set of equations (2) to an approximate coupled pair^{1–3} for N_{av} and N_1 :

$$dN_1/dt \approx R(1 - \theta) - hK_{av}(N_1^*) N_{av} \quad (4a)$$

$$dN_{av}/dt \approx (1 - \theta)hK_i \exp[E/(k_B T)](N_1^*)^{i+1} \quad (4b)$$

where $K_{av} = \sum_{s>i} K_s N_s / \sum_{s>i} N_s \sim (s_{av})^{-1} \sum_{s>i} K_s F(s/s_{av}, \theta)$ is the average capture number for stable islands. Analysis of (4) reveals a “short” transient regime, where N_1 rapidly builds up.^{1–3} This is followed by a “steady-state” regime, where the gain in N_1 due to deposition is roughly balanced by the loss primarily due to aggregation to islands, so one has $dN_1/dt \approx 0$ or $\dot{N}_1^* \approx R(1 - \theta)/(hK_{av}N_{av})$. This result

(30) Šmilauer, P.; Vvedensky, D. D. *Phys. Rev. B* **1995**, *52*, 14263.

(31) Bartelt, M. C.; Evans, J. W. *Phys. Rev. Lett.* **1995**, *75*, 4250.

(32) Evans, J. W.; Sanders, D. E.; Thiel, P. A.; DePristo, D. E. *Phys. Rev. B* **1990**, *41*, 5410. Evans, J. W. *Phys. Rev. B* **1991**, *43*, 3897. Sanders, D. E.; Evans, J. W. In *The Structure of Surfaces III*; Tong, S. Y.; van Hove, M. A.; Takayanagi, K.; Xie, X. D. Eds.; Springer-Verlag: Berlin, 1991; Vol. 24.

(33) Egelhoff, W. F., Jr.; Jacob, I. *Phys. Rev. Lett.* **1989**, *62*, 921. Nyberg, G. L.; Kief, M. T.; Egelhoff, W. F. *Phys. Rev. B* **1993**, *48*, 14509. (34) Flynn, D. K.; Evans, J. W.; Thiel, P. A. *J. Vac. Sci. Technol. A* **1989**, *7*, 2162 (1989).

(35) Kang, H. C.; Evans, J. W. *Surf. Sci.* **1992**, *269/270*, 784.

(36) Family, F.; Meakin, P. *Phys. Rev. Lett.* **1988**, *61*, 428. *Phys. Rev. A* **1989**, *40*, 3836.

(37) Bartelt, M. C.; Evans, J. W. *Phys. Rev. B* **1992**, *46*, 12675. Bartelt, M. C.; Tringides, M. C.; Evans, J. W. *Phys. Rev. B* **1993**, *47*, 13891.

Table 1. h/R -Dependence of N_{av} and N_1 and Estimates of the Exponents χ and ω for $h/R \approx 10^8$ ^a

h/R	$N_{av}^{(SIM)} (i=1)$	$N_1^{(SIM)} (i=1)$	$N_{av}^{(BC)} (i=1)$	$N_1^{(BC)} (i=1)$	$N_{av}^{(SIM)} (i=2)$	$N_1^{(SIM)} (i=2)$	$N_{av}^{(BC)} (i=2)$	$N_1^{(BC)} (i=2)$
10^4	1.19E-2	3.09E-3	1.07E-2	1.92E-3	7.48E-3	5.14E-3	5.91E-3	9.14E-3
10^5	7.27E-3	6.73E-4	5.95E-3	3.96E-4	3.08E-3	1.38E-3	2.18E-3	2.18E-3
10^6	3.86E-3	1.46E-4	2.97E-3	8.36E-5	1.13E-3	4.06E-4	7.60E-4	6.07E-4
10^7	1.92E-3	3.25E-5	1.40E-3	1.80E-5	3.98E-4	1.30E-4	2.58E-4	1.77E-4
10^8	9.21E-4	6.93E-6	6.50E-4	3.92E-6	1.40E-4	4.20E-5	8.53E-5	5.34E-5
	$\chi^{(SIM)}$	$\omega^{(SIM)}$	$\chi^{(BC)}$	$\omega^{(BC)}$	$\chi^{(SIM)}$	$\omega^{(SIM)}$	$\chi^{(BC)}$	$\omega^{(BC)}$
	~ 0.32	~ 0.67	$0.33 \approx 1/3$	$0.66 \approx 2/3$	> 0.45	~ 0.50	$\geq 0.48 \approx 1/2$	$\leq 0.52 \approx 1/2$

^a We show results from simulations of square islands [SIM] of critical size $i=1$ at 0.05 ML, and $i=2$ with $E_2=0$ at 0.1 ML, and from corresponding rate equations using Bales-Chrzan K_s [BC]. For the same parameters, rate equations using constant $p=q=1/2$, yield exponents $\chi \approx 0.31 \approx 1/3$ and $\omega \approx 0.69 \approx 2/3$ for $i=1$, and $\chi \approx 0.43 \approx 5/11$ and $\omega \approx 0.58 \approx 6/11$ for $i=2$.

can be substituted into the N_{av} -rate equation in (4b), which can then be integrated given K_{av} (and K_i). We now discuss various choices for the K_s and determine the associated basic scaling exponents, χ and ω , where $N_{av} \sim R^\chi$ and $N_1 \sim R^\omega$, at fixed T and θ .

II.1. Idealized Choices of Capture Numbers K_s . (A) **Constant $K_s = K$** , so $K_{av} = K$. We motivate this traditional choice¹⁻³ with the observation that diffusing adatoms execute 2D space-filling random walks, so their capture by islands should *not* depend strongly on their size (at least for well-separated islands at low θ). This choice produces the *conventional scaling*¹⁻³ (1)

$$\chi = i/(i+2) \text{ and } \omega = 2/(i+2), \text{ so } \chi + \omega = 1 \quad (5)$$

the latter following from the steady-state relation $(h/R)KN_{av}N_1 \approx 1$.

(B) **$K_s \sim s^p N_{av}^q$ for $s > i$, with constant p and q , and $K_{s \leq i} = O(1)$** , so $K_{av} = \theta^p N_{av}^{q-p} \int dx x^p F(x)$, ignoring the θ -dependence of the island size scaling function, $F(\theta)$. Blackman and Wilding³⁸ considered the choice $p > 0$ and $q = 0$ (so $K_s \sim s^p$), attempting to describe perimeter-length mediated capture (so $p \approx 1/2$ for compact islands). The more general choice, $p > 0$ and $q > 0$ (in particular $p = q > 0$), is motivated by the work of Ratsch *et al.*¹⁴ Limitations of these choices are discussed below. In the general case, integration of (4) yields

$$\chi = i/[(i+2) - (i+1)(p-q)] \quad (6a)$$

$$\omega = (2+q-p)/[(i+2) - (i+1)(p-q)] \quad (6b)$$

for $p \leq 1/(i+1)$, and

$$\chi = (i+1-p)/[(i+3) - (i+1)(p-q) + q] \quad (7a)$$

$$\omega = (2+q-p)(1+p)/[(i+3) - (i+1)(p-q) + q] \quad (7b)$$

for $p \geq 1/(i+1)$. In either case, one has $(1+q-p)\chi + \omega = 1$, which follows from the steady-state relation $(h/R)K_{av}N_{av}N_1 \approx 1$. Other $\chi(p,q)$ and $\omega(p,q)$ forms result for different choices of K_i (see ref 39).

We remark that the case $p \geq 1/(i+1)$ is complicated by the feature that the “rapid” decrease of K_{av} to zero, as $\theta \rightarrow 0$, creates a divergence in the integration of the N_{av} -rate equation. In fact, this equation should only be integrated back to the beginning of the steady-state regime, $\theta \approx \theta_{min}$. One alternative approach here matches transient regime behavior, $N_{av} \approx (i+2)^{-1}K_i(h/R) \times \exp[E/(k_B T)]\theta^{i+2}$ and $N_1 \approx \theta$, to steady-state behavior, $N_{av} \approx R/(hK_{av}N_1)$, when $\theta = \theta_{min}$. This determines the scaling of θ_{min} and $N_{av}(\theta = \theta_{min})$. We have shown that the latter coincides with N_{av} scaling at fixed θ , and reproduces (7).

II.2. Realistic Choices for Capture Numbers K_s . (A) **Bales and Chrzan**⁴⁰ (BC) K_s values were obtained by analyzing the diffusion equation for *irreversible* capture of adatoms at circular islands of radii $R_s \approx (2\pi)^{-1/2}s^{1/2}$, with an *approximate* treatment of the “stochastic background” of other islands. One finds that

$$K_s = g(R_s/L_{av}) \text{ with } g(y) \equiv 2\pi y \mathcal{K}_1(y)/\mathcal{K}_0(y) \quad (8)$$

where the \mathcal{K}_n are modified Bessel functions of order n . Thus $g(y) \sim 1/|\ln(y)|$, as $y \rightarrow 0$, and $g(y) \sim y$, for larger y . Noting that $sN_{av} = 2\pi(R_s/L_{av})^2$, it immediately follows that $K_s = k(sN_{av})$, corresponding to “ $p = q$ ” in the formalism (B) of section II.1. Here $k()$ is a scaling function satisfying $k(x) \sim 1/|\ln(x)|$, as $x \rightarrow 0$, and $k(x) \sim x^{1/2}$, for larger x , so “ $p = q \rightarrow 0$ ”, as $\theta \rightarrow 0$, and “ $p = q \approx 1/2$ ”, for higher θ .

Although the BC analysis was for $i=1$, it is clear that their results for K_s apply also for irreversible capture by *stable* islands for any $i > 1$. Integration of the N_{av} rate equation in (4b) is free of divergence since $K_{av} = K_{av}(\theta) = \int dx k(x\theta)F(x,\theta) \sim 1/|\ln(\theta)| \rightarrow 0$ so slowly, as $\theta \rightarrow 0$, and produces conventional scaling (1). Clearly, the BC K_s values do not apply for higher θ where coalescence is significant; however presumably N_{av} scaling is already “locked in” by this stage.

(B) **Generic Form for the K_s** . Since the BC form derives from a circular island geometry and incorporates only an approximate treatment of the “background islands”, it is appropriate to search for a generic form. This would hopefully incorporate the essential features of the *exact* capture numbers for general compact island geometries. We propose⁴¹ $K_s \sim (sN_{av})^{p(x)}$, where $p(x) \sim 1/|\ln(x)| \rightarrow 0$ as $x \rightarrow 0$, and $p(x) \approx 1/2$ for larger x . Thus K_s values are effectively independent of s ($p \approx 0$) for low θ but reflect perimeter-mediated capture ($p \approx 1/2$) at higher θ .

We remark that conventional scaling (5) is in fact found in simulations of nucleation and growth of compact islands with *prescribed* critical size¹¹ $i \geq 1$ (model A in section I), as shown in Table 1, or with prescribed bond-breaking¹² (model B in section I). This is expected from the above extension of the BC analysis. It is instructive to note that this behavior is not produced by choosing $K_s \sim s^p$, with $p = 1/2$, for any $i \geq 1$ [see (6) and (7)], or even by choosing $K_s \sim s^p N_{av}^q$, with $p = q = 1/2$, for any $i \geq 2$ [see (7)].

II.3. Random Walk Formulation of Adatom Capture by Islands. On the basis of random walk theory, we have replaced^{11,37} the term $hK_s N_s N_1$, for the total rate of aggregation of isolated adatoms with islands of size s , with $P_s \bar{N}_i / \tau_s$. Here $P_s \sim N_s / N_{av}$ is the probability to deposit in the vicinity of an island of size s , and τ_s gives the mean time for an atom deposited on a finite lattice of $1/N_{av}$ sites (with periodic boundary conditions) to diffuse and reach

(38) Blackman, J. A.; Wilding, A. *Europhys. Lett.* **1991**, *16*, 115.

(39) For example, for $K_i \sim i^p N_i^q$, one finds $\chi = i/[(i+2) - (i+1)(p-q)]$ for $p \leq 1/(i+1)$, and $\chi = (i+1-p)/[(i+3) - (i+1)(p-q) - pq]$ for $p \geq 1/(i+1)$, with $(1+q-p)\chi + \omega = 1$ in either case.

(40) Bales, G. S.; Chrzan, D. C. *Phys. Rev. B* **1994**, *50*, 6057.

(41) Bartelt, M. C.; Evans, J. W. *Surf. Sci.* **1994**, *314*, L835.

for the first time an island of s atoms placed on the lattice. This formulation recovers, e.g., the behavior $K_1 \sim 1/|\ln(N_{av})|$ from the N_{av} dependence of τ_s , entirely consistent with (8). It also has the advantage of naturally extending to treat anisotropic or one-dimensional adatom diffusion,^{37,42} and even “anomalous” diffusion.⁴³

II.4. Natural Rescaling of Island and Adatom Densities. Examination of the rate equations (4) for low $\theta \ll 1$ and constant K_s suggests the natural rescaled variables

$$\hat{\theta} = \theta (h/R)^{-2/(i+3)} \sim \theta/\theta_{\min} \quad (9a)$$

$$\hat{N}_1 = N_1 (h/R)^{-2/(i+3)} \quad (9b)$$

$$\hat{N}_{av} = N_{av} (h/R)^{-(i+1)/(i+3)} \quad (9c)$$

satisfying

$$\hat{N}_{av} \approx (i+2)^{1/(i+2)} \exp[(i+2)^{-1} E_i/(k_B T)] (\hat{\theta})^{1/(i+2)} \quad \text{and} \quad \hat{N}_1 \hat{N}_{av} \approx 1 \quad (10)$$

This generalizes Tang’s rescaling⁴⁴ for $i=1$. The “clean” temporal scaling $N_{av} \sim t^{1/(i+2)}$ in (10) is observed for nucleation and growth of “point islands”³⁷ (occupying a single site), but *not* in practice for compact islands, where N_{av} “quickly saturates” (as, e.g., demonstrated by rate equations including the full θ -dependence of rates for various processes^{11,40}). However, the “point island” temporal scaling does in a certain sense control the h/R -scaling for compact islands. This is best demonstrated in plots of \hat{N}_{av} (and \hat{N}_1) versus $\hat{\theta}$ (see Figure 1). These clearly show that the $\hat{N}_{av} \sim \hat{\theta}^{1/(i+2)}$ curves for “point islands” (for large h/R) provide an *envelope* for the corresponding curves for compact islands. This enforces the same asymptotic h/R -scaling behavior, at *fixed* θ , for both “point” and compact islands.

II.5. Island Size and Separation Distributions. Next we consider the full *island size distribution*. Specifically, we compare predictions of the rate equations (2), using the most sophisticated BC choice of capture numbers, with exact simulation results using our model for nucleation and growth of square islands¹¹ mimicking metal(100) homoepitaxy. In Figure 2 we show results for the scaling function, $F(x, \theta)$ defined in (3), for the case $i=1$ at low θ . The rate-equation predictions reasonably match the “exact” simulation results for typical h/R . However, it seems that the true asymptotic ($h/R \rightarrow \infty$) scaling function might be analytic for the exact simulation model, but nonanalytic and discontinuous for the rate equations (cf. the “point-island” analysis in ref 37). This points to a fundamental limitation of the neglect of fluctuations in the mean-field rate-equation approach.⁴⁵

Both rate-equation and simulation studies show that the scaling function becomes narrower and taller with increasing critical size, i . A generic analytic form, $F_i = C_i x^i \exp[-ia_i x^{1/a_i}]$, with i -dependent constants a_i and C_i , has been proposed for this dependence.¹² However, it does not capture the feature that $F_i(x=0) > 0$, which we believe applies for nucleation and growth of compact islands.^{3,11}

Finally, we note that islands formed by these nucleation and growth processes are not distributed “randomly” on the surface. Rather, examination of the *island separation distribution* shows that there is a depletion in the population of nearby pairs of islands, which is actually

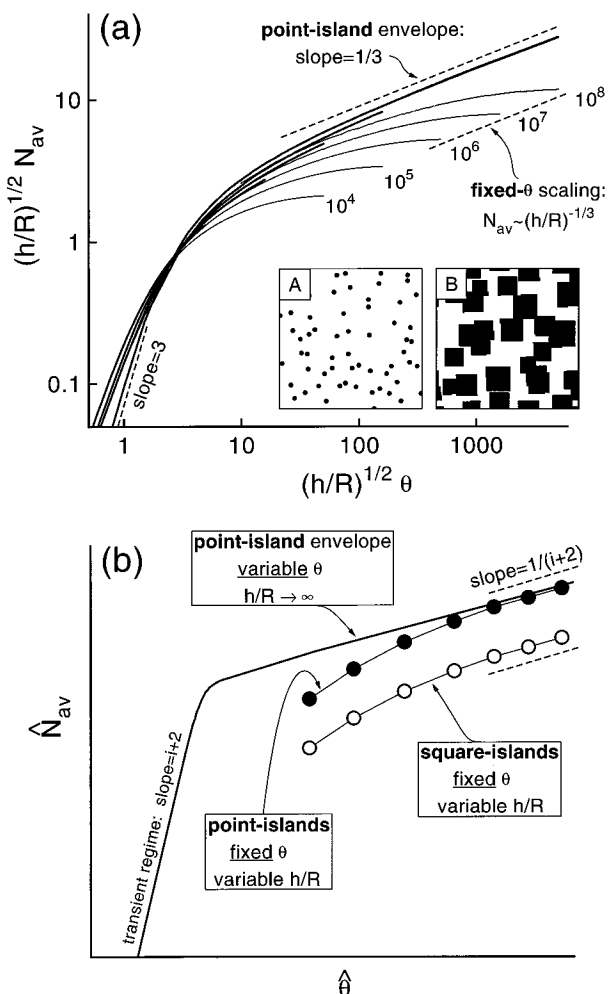


Figure 1. Behavior of $\hat{N}_{av} = (h/R)^{-(i+1)/(i+3)} N_{av}$ versus $\hat{\theta} = (h/R)^{2/(i+3)} \theta \propto \theta/\theta_{\min}$, for isotropic diffusion. In (a) we show simulation data for $i=1$, in the range $10^4 \leq h/R \leq 10^8$, as indicated, and $\theta \leq 0.5$ ML. Thin solid lines correspond to simulations of *square islands*, and thick lines to “*point islands*”. Insets A and B show pictures of the adlayer from simulations of “point” and square islands, respectively, with $h/R = 10^8$ and $\theta = 0.5$ ML. In (b) we give a schematic of expected behavior for general i on a log-log plot of \hat{N}_{av} versus $\hat{\theta}$.

enhanced with increasing i (see refs 1–3, 11, and 46). Since the edges of stable islands act as sinks for diffusing adatoms, the isolated adatom density is depleted nearby islands. Consequently, the probability of nucleating an island in the “vicinity” of an existing island is reduced. This effect was observed in simulations^{3,11,46} but also follows from diffusion-equation analyses.^{1,2,46}

III. Transitions in Critical Size with Increasing Temperature

For sufficiently low T , the critical size, i , for stable islands clearly must be unity, i.e., all islands are effectively stable against dissociation.^{1–3} However, increasing T so that bond breaking becomes operative should lead to an increase in i . For “high” T , one might anticipate some effective “large” i above which islands are more likely to grow than to shrink, rather than being absolutely stable.¹ The traditional view is that (1) still applies with this i and can be used to extract energies.¹ However, recent simulation studies of the pair-interaction model, (C) in section I, which does not prescribe i , have suggested a breakdown in scaling (1) once bond-breaking becomes

(42) Bartelt, M. C.; Evans, J. W. *Europhys. Lett.* **1993**, *21*, 99.

(43) Liu, S.; Böning, L.; Detch, J.; Metiu, H. *Phys. Rev. Lett.* **1995**, *74*, 4495.

(44) Tang, L.-H. *J. Phys. I* **1993**, *3*, 935.

(45) Bartelt, M. C.; Evans, J. W. *Bull. Am. Phys. Soc.*, in press.

(46) Evans, J. W.; Bartelt, M. C. *Surf. Sci.* **1993**, *284*, L437.

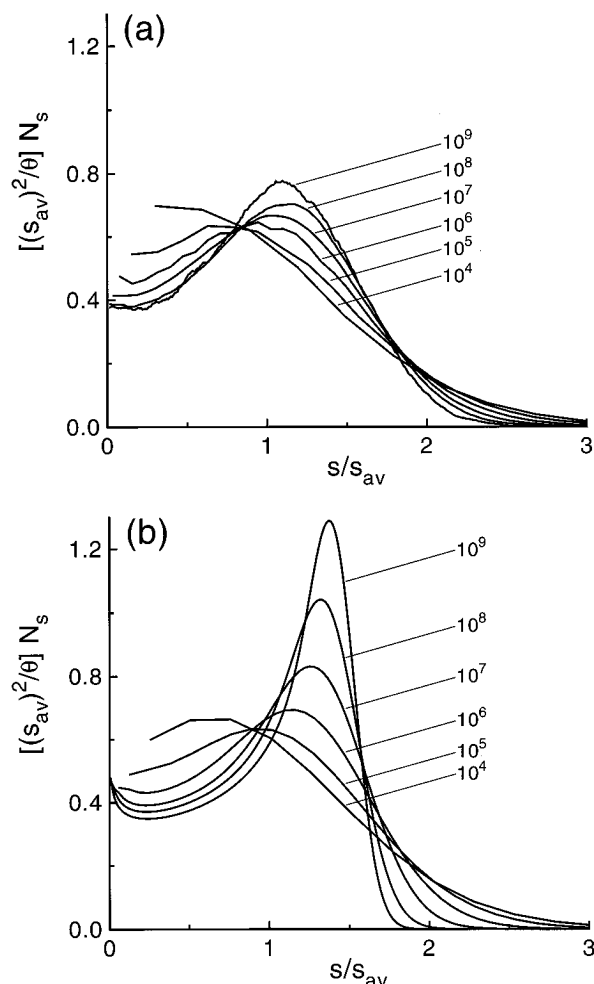


Figure 2. Island size distributions with $i=1$, obtained at 0.05 ML, for $10^4 \leq h/R \leq 10^9$, from (a) simulations of square islands, and (b) numerical integration of rate equations with BC capture numbers.

operative.^{14,15} We wish to clarify this issue, and at the same time provide a precise characterization of transitions between “small discrete” critical sizes for unreconstructed metal(100) homoepitaxy,¹⁶ in the experimentally relevant range of “lower” T and “small” i .

III.1. Energetics and Kinetics of Island Dissociation. Details of critical size variation with T depend on the effective rates for dissociation (i.e., removal of a perimeter atom) from islands of various sizes, s . (Here these islands are assumed to have their most stable configuration.) We denote the associated effective activation barriers by $E_{\text{diss}}(s) > 0$. If the total binding energy of the island is given by $E_b(s) > 0$, then $\delta E_b(s) = E_b(s) - E_b(s-1) - E_b(1)$ gives the net change in binding energy upon “fully” separating an adatom from the island, and $\delta E_b(2) = E_{\text{bond}}$ corresponds to the previously introduced bond energy between adatoms in a surface dimer. Then typically one has

$$E_{\text{diss}}(s) = \delta E_b(s) + E_d \quad (11)$$

Note that, in general, there will be several pathways, ρ , for fully separating or dissociating an adatom from an island, each involving a few steps with barriers typically distinct from E_d or $E_{\text{diss}}(s)$. Let $E_{\rho}(s)$ denote the height of the largest barrier (above the initial energy) for each dissociation pathway, ρ , and let $E_{\text{bar}}(s) = \min_{\rho} \{E_{\rho}(s)\}$ denote the minimum of these over all pathways. Then the effective dissociation barrier, $E_{\text{diss}}(s)$, is the maximum

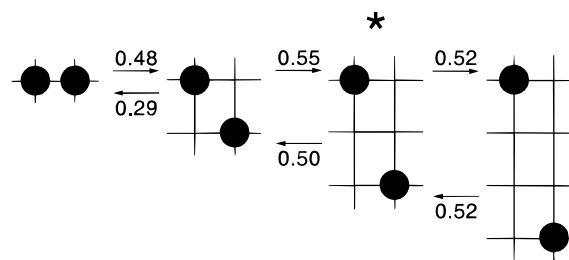


Figure 3. MD/MC-CEM estimates (in eV) of activation barriers for each step during dissociation of Cu dimers on Cu(100) (L. S. Perkins, unpublished). For the pathway (ρ) shown, $E_{\rho}(2) = E_{\text{bar}}(2) \approx 0.55$ eV is only slightly larger than $E_d \approx 0.52$ eV. $H_{\text{diss}}(2)$ is calculated as the product of the (relative) quasi-equilibrium concentration, $\exp[-\delta E_b(2)/(k_B T)]$, of the almost fully dissociated dimer (*), and the hop rate, h , for the last dissociation step. Note that the MD/MC-CEM barrier for dimer diffusion (0.48 eV) is lower than that for monomer diffusion (0.52 eV), inconsistent with the analysis of section VI.

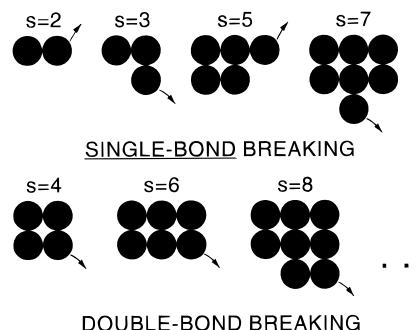


Figure 4. Schematic of dissociation of adatoms from compact cluster configurations.

of $E_{\text{bar}}(s)$ and $\delta E_b(s) + E_d$. The latter is normally much larger for metal homoepitaxy, leading to (11). See Figure 3.

Insight into transitions in critical size follows directly from appropriate comparison of dissociation energies. One expects that $\delta E_b(s) \geq \delta E_b(2)$, so $E_{\text{diss}}(s) \geq E_{\text{diss}}(2)$, and thus all islands are stable if dimers are stable (corresponding to $i=1$ at low T). We also expect that $\delta E_b(2) \approx \delta E_b(3) \approx \delta E_b(5) \approx \delta E_b(7)$, since dissociation of islands of sizes $s=2, 3, 5, 7$ shown in Figure 4 requires just “single-bond breaking”, but that all other $\delta E_b(s) \approx \delta E_b(4)$ are substantially higher, since dissociation here requires “double-bond breaking”. MD/MC-CEM and EAM calculations^{16–18} support these claims. Thus, with increasing T , one might expect a jump directly from critical size $i=1$ to an unconventional $i=3$. (The $i=3$ regime is unconventional in that not all islands of size $s > 3$ are stable.)

III.2. Crossover Analysis. One expects that the crossover from $i=1$ should be determined by the relative magnitudes of the rate of dimer dissociation, $H_{\text{diss}}(2) \sim \nu \exp[-(E_d + E_{\text{bond}})/(k_B T)]$, and the rate, $H_{\text{agg}}(2) \sim hK_2N_1$, at which adatoms aggregate with and “stabilize” dimers by creating larger, more stable, doubly-bonded islands.¹⁶ Thus a natural “crossover variable” is the ratio $\mathcal{R} = H_{\text{diss}}(2)/H_{\text{agg}}(2)$, but it is more useful to choose $Y = (\nu/R) \exp[-(E_d + 3E_{\text{bond}}/2)/(k_B T)]$. Note that $\mathcal{R} \sim Y^{2/3}$ when $i=1$ and $\mathcal{R} \sim Y^{2/5}$ when $i=3$ is always a simple function of Y . Indeed, a simple rate-equation analysis incorporating single-bond breaking (but artificially excluding double-bond breaking) indicates clean $i=1$ scaling of N_{av} for $Y \lesssim 1/50$, crossing over to clean $i=3$ scaling for $Y \gtrsim 50$. Thus we can identify the upper- T limit of the $i=1$ regime, T_{1+} , by the condition $Y(T = T_{1+}) \approx 1/50$, and the lower- T limit of the $i=3$ regime, T_{3-} , by $Y(T = T_{3-}) \approx 50$. Note that classic $i=3$ scaling occurs for high T despite the fact

that certain islands of size $s > 3$ are not stable. Analogous behavior has been observed in simulation studies.⁴⁷

In reality, the $i = 3$ regime is limited by the onset of double-bond breaking.^{15,16} For $i = 3$ behavior to apply, it is certainly *sufficient* that double-bond breaking be negligible on the time scale of the experiment. Roughly, this implies that $H_{\text{diss}}(4) < R$. A more refined criterion is derived in ref 16. [The weaker condition that double-bond breaking be negligible on the time scale of aggregation, i.e., that $H_{\text{diss}}(4) < H_{\text{agg}}(4) = hK_4N_1$ is *not* sufficient. Aggregation with tetramers does not lead to the formation of more stable islands.] The condition that $H_{\text{diss}}(4) = \nu \exp[-(E_d + \delta E_b(4))/(k_B T)] \approx R$ can be used to crudely estimate the upper- T limit of the $i = 3$ regime, T_{3+} . In the special case where $\delta E_b(4) = 2\delta E_b(2) = 2E_{\text{bond}}$, one can combine the criteria for T_{3-} and T_{3+} to obtain

$$T_{3+}/T_{3-} \approx 1 + \sigma(2 + 3\sigma)^{-1}, \quad \text{where } \sigma = E_{\text{bond}}/E_d \quad (12)$$

Thus a "well-defined" regime of $i = 3$ (i.e., extending over a significant temperature range) will only be observed if the key parameter $\sigma = E_{\text{bond}}/E_d$ is not too small. These ideas are applied to analyze behavior of Fe/Fe(100) and Cu/Cu(100) epitaxy in section VI, where we report associated values of E_d and E_{bond} , as well as transition temperatures T_{1+} , T_{3-} , and T_{3+} .

This analysis clarifies recent simulation results^{14,15} for the pair-interaction model, (C) in section I, which suggested the breakdown of classic scaling and the lack of well-defined critical sizes for $i > 1$. These studies were indeed performed assuming $\delta E_b(4) = 2\delta E_b(2)$, as above, and which is reasonable for metal(100) homoepitaxy.¹⁶ However, they focused on *small* values of σ (for higher T) and thus saw no well-defined $i = 3$ regime.¹⁵ Such $i = 3$ behavior would no doubt emerge for larger σ , or for $\delta E_b(4)$ sufficiently larger than $2\delta E_b(2)$. In any case, a key insight from these studies is that, even for larger σ , one should expect a broad crossover range of temperatures between $i = 1$ and $i = 3$ scaling (i.e., between T_{1+} and T_{3-}). Reference 15 further found that the shape of the island size distribution in the transition region was naturally parameterized by \mathcal{R} (or one could use \mathcal{Y}). Finally, we emphasize that, even for larger σ , the classic scaling (1) cannot be applied directly when $1 < i < 3$. Instead, a suitable interpolation formula must be used.¹⁶

It is appropriate to note that when $T > T_{3+}$ (square tetramers are unstable due to double-bond scission), one expects dissociation of all islands to also be operative, so one should not expect well-defined regimes of integer critical size $i > 3$ (cf. ref 15). Certainly (1) can be used to estimate energies treating i as an output parameter obtained from flux scaling,⁴⁸ but the precision of such estimates has yet to be rigorously investigated.

Finally, we mention that critical size behavior depends on the adsorption site geometry. Consider a system with a triangular lattice of adsorption sites [e.g., the fcc adsorption sites on a fcc(111) surface]. For strong adatom-adatom bonding, one might expect a transition from $i = 1$ (all islands are stable) to $i = 2$ (doubly bonded triangular trimers are stable) to $i = 6$ scaling (triply bonded pentamers are stable), but also expect no well-defined regimes of integer $i > 6$.

IV. Transition to Multilayer Growth: Real-Space Morphology

Let us first introduce basic quantities characterizing film structure.^{4,5,25} We label layers by an index $j = 0, 1$,

2, ..., with $j = 0$ denoting the substrate. Let θ_j denote the coverage of layer j , and $P_j = \theta_j - \theta_{j+1}$ denote the average fraction of *surface* (or exposed) atoms in layer j . Then one has $\sum_{j \geq 0} P_j = 1$, $\theta_j = P_j + P_{j+1} + P_{j+2} + \dots$ (so $\theta_0 = 1$), and $\theta = \sum_{j \geq 1} \theta_j = \sum_{j \geq 0} j P_j = j_{\text{av}}$. The basic measure of film roughness is the interface width, W , which satisfies $W^2 = \sum_{j \geq 0} (j - j_{\text{av}})^2 P_j$.

We also introduce the probabilities, $P_{ij}(\delta \mathbf{l})$, for finding two *surface* atoms in layers i and j , separated *laterally* by the vector $\delta \mathbf{l}$. These generate the height-difference distributions, $G_n(\delta \mathbf{l}) = \sum_{j-i=n} P_{ij}(\delta \mathbf{l})$, for finding *surface* atoms separated laterally by $\delta \mathbf{l}$, with a height difference $n = 0, \pm 1, \dots$. By symmetry, $G_n(\delta \mathbf{l}) = G_n(-\delta \mathbf{l}) = G_{-n}(\delta \mathbf{l})$, for all n and $\delta \mathbf{l}$. Finally, we introduce the height-height correlation function or mean square height-difference $H(\delta \mathbf{l}) = \sum_n n^2 G_n(\delta \mathbf{l})$, for lateral separation $\delta \mathbf{l}$. Note that trivially $H(\mathbf{0}) = 0$ and $H(\infty) = 2W^2$, since $P_{ij}(\delta \mathbf{l}) \rightarrow P_i P_j$ as $|\delta \mathbf{l}| \rightarrow \infty$. Strictly, the above notation applies only for an unphysical simple-cubic geometry since, in realistic fcc(100) and bcc(100) geometries, one should distinguish several types of surface atoms covered to various degrees by higher layer atoms.⁴⁹ However, we ignore this complication here. We also note that an alternative notation for simple cubic geometries is available (see ref 50).

IV.1. Submonolayer or Layer-by-Layer Growth. Consider submonolayer growth with no higher layer population, or more generally layer-by-layer growth. If $\theta = k + \delta\theta$, where $0 \leq \delta\theta < 1$ (so $k = 0$ for the submonolayer case), then $P_k = 1 - \delta\theta$ and $P_{k+1} = \delta\theta$ are the only nonzero P_j 's, and one has $W^2 = \delta\theta(1 - \delta\theta)$. Also, the only nonzero $G_n(\delta \mathbf{l})$'s are G_0 and $G_{+1} = G_{-1}$, which satisfy $G_0 = 1 - 2G_{+1}$. Here these G_n are completely determined by $H(\delta \mathbf{l}) = 2G_{+1}(\delta \mathbf{l})$. Furthermore, $C(\delta \mathbf{l}) = \frac{1}{2}[H(\infty) - H(\delta \mathbf{l})]$ corresponds to the usual two-point correlation function for the partially filled layer.¹¹

The typical form of $H(\delta \mathbf{l})$ for submonolayer nucleation and growth reflects the island distribution and specifically the average island separation, $l_{\text{av}} = (N_{\text{av}})^{-1/2}$. $H(\delta \mathbf{l})$ first increases linearly, with slope $\propto \delta\theta/l_{\text{av}}$, and then "overshoots" before reaching the asymptotic value of $2W^2 = 2\delta\theta(1 - \delta\theta)$. See Figure 5a. The linear increase reflects intralayer correlations. The overshoot feature is due to "depletion effects": for $\delta l < l_{\text{av}}$ somewhat larger than the typical linear island size, $(\delta\theta)^{1/2} l_{\text{av}}$, there is enhanced likelihood of a maximum height difference of unity due to one point coinciding with an island and the other being in the surrounding depletion zone.¹¹

IV.2. Rough Multilayer Growth. We have noted that kinetic roughening²⁵ is generally characterized by an increase in the interface width, W , with increasing coverage or mean film height, θ , of the form $W \sim \theta^\beta$. It is convenient to write⁵¹

$$P_j \approx W^{-1} f(j - \theta/W) \quad (13)$$

where

$$\int dx f(x) = \int dx x^2 f(x) = 1 \quad \text{and} \quad \int dx x f(x) = 0$$

Here f gives the shape of the film height distribution. The constraints on f follow by recalling that the P_j distribution is normalized with mean θ and variance W^2 . It will be

(49) Kang, H. C.; Flynn-Sanders, D. K.; Thiel, P. A.; Evans, J. W. *Surf. Sci.* **1991**, *256*, 205.

(50) In terms of height variable, $h(\mathbf{l})$, for the surface at *lateral* position \mathbf{l} , if $\langle \rangle$ denotes an ensemble average, then one has $\theta = \langle h(\mathbf{l}) \rangle$, $W^2 = \langle [h(\mathbf{l}) - \langle h(\mathbf{l}) \rangle]^2 \rangle$, $H(\delta \mathbf{l}) = \langle [h(\mathbf{l} + \delta \mathbf{l}) - h(\mathbf{l})]^2 \rangle$, and $C(q, \delta \mathbf{l}) = \langle \exp[iq \cdot (h(\mathbf{l} + \delta \mathbf{l}) - h(\mathbf{l}))] \rangle$.

(51) Kang, H. C.; Evans, J. W. *Surf. Sci.* **1992**, *271*, 321. Evans, J. W. *Phys. Rev. B* **1989**, *39*, 5655.

(47) Schroeder, M.; Wolf, D. E. *Phys. Rev. Lett.* **1995**, *74*, 2062.

(48) Venables, J. A. *Phys. Rev. B* **1987**, *36*, 4153.

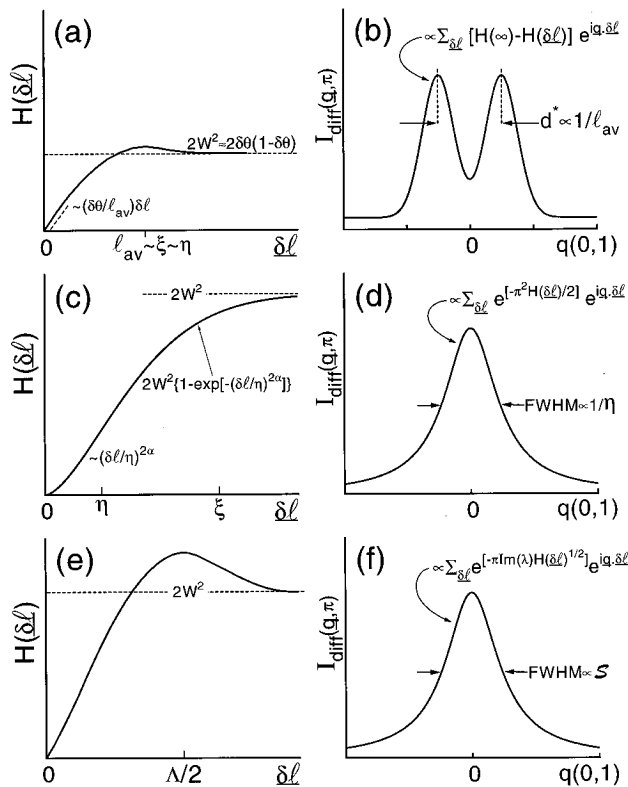


Figure 5. Schematic of the behavior of the height–height correlation function, $H(\delta l)$, for lateral separation δl , associated with (a) quasi-layer-by-layer (or submonolayer) growth, (c) the traditional multilayer kinetic roughening model of self-affine growth, (e) the observed behavior in our multilayer growth model with a Schwoebel barrier. In (b), (d), and (f), we show schematics of the corresponding (antiphase) kinematic diffraction profiles.

instructive to note that for a general distribution f , one can always develop a cumulant expansion⁵² for $\tilde{f}(k) = \int dx e^{ikx} f(x)$, such that $\ln[\tilde{f}(k)] = \sum_{m \geq 0} (ik)^m \kappa_m / m!$. For the distribution in (13), the cumulants, κ_m , satisfy $\kappa_0 = \int dx f(x) = 1$, $\kappa_1 = \int dx x f(x) = 0$, $\kappa_2 = \int dx x^2 f(x) = 1$, $\kappa_3 = \int dx x^3 f(x)$ (which measures the skewness), etc. Since the height-difference distributions, $G_n(\delta l)$, are normalized, even, and have variance $H(\delta l)$, we also naturally write

$$G_n \approx H^{-1/2} g(n/H^{1/2}) \quad (14)$$

with even g satisfying

$$\int dy g(y) = \int dy y^2 g(y) = 1$$

We now describe behavior of the two basic paradigms for kinetic roughening mentioned in Section I:

(A) Self-affine growth models are discussed first, for completeness and contrast. The locally self-affine structure of the growing film produces the “short-separation” scaling behavior²⁵

$$H(\delta l) \sim (\delta l/\eta)^{2\alpha}, \quad \text{for } l_0 \ll \delta l \ll \xi \quad (15)$$

before crossing over to $H(\delta l) \approx 2W^2$, for $\delta l \gtrsim \xi$. Here l_0 is a short-range cutoff, and η is a time-invariant constant.⁵ The parameter ξ is a measure of the (total) lateral correlation length, and must satisfy $W \sim (\xi/\eta)^\alpha \sim \theta^\beta$. If this relation applies for $\theta = O(1)$, where $\xi \approx l_{av}$, then one

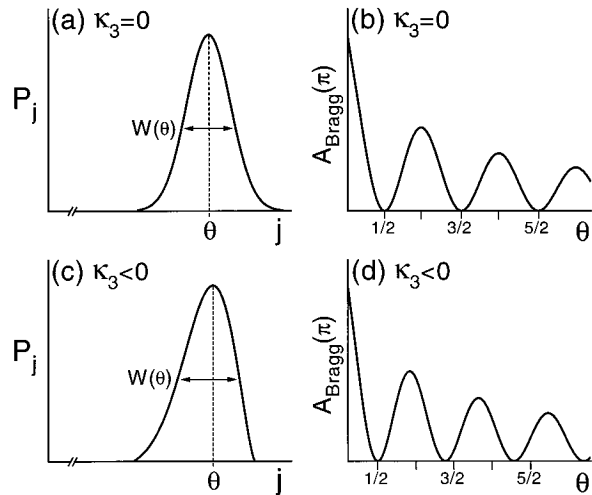


Figure 6. Schematic of the behavior of the film height distribution, P_j , versus j , for (a) Gaussian ($\kappa_3 = 0$) and (d) skewed-Gaussian (with $\kappa_3 < 0$) P_j -forms. In (b) and (d) we show schematics of the corresponding $A_{\text{Bragg}}(\pi)$ versus θ .

has $\eta \sim l_{av}$, i.e., l_{av} determines the *time-invariant* constant, η , which characterizes subsequent rough growth.

We note that $H(\delta l)$ is often approximated by the monotonically increasing form^{5,25} $H(\delta l) \approx 2W^2\{1 - \exp[-(\delta l/\xi)^{2\alpha}]\}$. See Figure 5c. Also, it is invariably either implicitly or explicitly assumed that both P_j and G_n are described by Gaussian distributions (but see ref 53).

(B) Unstable growth due to a step-edge barrier is a more appropriate paradigm than (A) for metal(100) homoepitaxy. Behavior here is characterized by the development of “mounds” with selected (or slowly-varying) slope. This corresponds most closely to $\alpha = 1$ in paradigm (A) above. These “mounds” are observed^{30,31,54} to coarsen slowly in time (t), with “base” width, Λ , increasing asymptotically like t^n , with $n = 0.16$ – 0.25 . Clearly, one has $\beta = n$ for strictly fixed mound slope. Studies by us³¹ and others³⁰ find that $H(\delta l)$ does *not* increase monotonically with δl , but rather develops damped oscillations, as might be expected for a disordered array of mounds. See Figure 5e. For very well-developed mounds with slope $S \propto W/\Lambda$, one expects that $H \sim [(\delta l)S]^2$, for $\delta l \ll \Lambda$, but discrete lattice effects inhibit the development of this quadratic form.

Our studies also show consistent deviation of the film height distribution, P_j , from a perfectly Gaussian form, reflecting a slight skewness corresponding to a negative third moment and cumulant,³¹ κ_3 . See parts a and c of Figures 6. For the height-difference distributions, G_n , we also find³¹ that a Gaussian fit is poorer than a rational fit, for the range of small ($< l_{av}$) lateral separations most relevant in determining the diffraction profile (see section V).

IV.3. Effect of Adsorption Site Geometry and Deposition Dynamics. For metal(100) homoepitaxy, where there is a “significant” step-edge barrier, we now comment on the influence of the 4-fold hollow (4FH) adsorption site geometry and of the downward funneling deposition dynamics. For a model with a simple-cubic geometry (and *no* transient mobility or knockout processes), one expects the roughness to increase monotonically with decreasing T , since it becomes progressively more difficult to surmount the step-edge barrier. In fact, as $T \rightarrow 0$, where thermal diffusion is inoperative, this

(53) Krug, J.; Meakin, P.; Halpin-Healy, T. *Phys. Rev. A* **1992**, *45*, 638.

(54) Strosio, J. A.; Pierce, D. T.; Stiles, M. D.; Zangwill, A.; Sander, L. M. *Phys. Rev. Lett.* **1995**, *75*, 4246.

(52) *Stochastic Processes in Physics and Chemistry*; van Kampen, N. G., Ed.; North-Holland: Amsterdam, 1981.

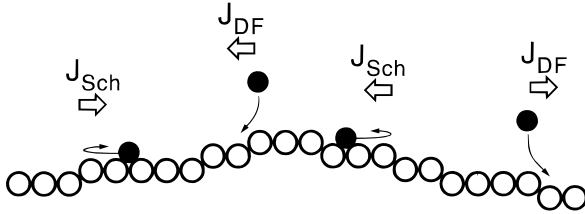


Figure 7. Schematic of the uphill (J_{Sch}) and downhill (J_{DF}) currents, associated with reflection at step-edge barriers and with downward funneling (DF), respectively.

model produces a very rough "Poisson" growth,⁵⁵ $P_j = \theta e^{-\theta/j}$, where $\beta = 1/2$. However, smooth growth is often observed in metal(100) homoepitaxy at low temperatures.^{33,34} This is a direct consequence of the 4FH adsorption site geometry, *together* with downward funneling during deposition. Indeed, simple random addition at 4FH sites alone produces substantially smoother growth⁵¹ with $\beta \approx 1/4$. (This model is unphysical in that atoms not impinging at 4FH sites do not adsorb, so the sticking probability is not unity.) The additional effect of downward funneling to 4FH sites (recovering a sticking probability of unity) results in even smoother growth⁵¹ with $\beta = 0$ or $W^2 \sim \ln(\theta)$, although actual behavior could be more complicated (see below).

This smooth growth at low T reflects the presence of a *downhill current* due to downward funneling to 4FH sites. Of course, this current is present at higher T , although it has reduced influence due to the lower step-edge density as a result of islanding. However, it plays a crucial role in counterbalancing the *uphill current* induced by the step-edge barrier and in determining mound morphology. See Figure 7. Thus the following overview emerges for the temperature dependence of roughening. Growth is smooth at low T due to the influence of downward funneling. Growth then first becomes rougher with increasing T , in a range where the step-edge barrier is insurmountable. This is due to the above mentioned *reduced influence* of downward funneling. If the islands become large enough, so that the downward funneling current is insignificant, *before* the step-edge barrier can be surmounted, then quasi-Poisson growth will be achieved. But, in general, the film becomes smoother again for higher T where the barrier becomes surmountable. We note that the above underlying mechanism for reentrant smooth growth during metal(100) homoepitaxy is different from the mechanism identified²¹ for metal(111) homoepitaxy.

Finally, we mention possible complications in the deposition dynamics not accounted for in the basic downward funneling model. Clearly, downward funneling will break down for impingement on large micropylramids, whose sides are (111) facets. In this case, incoming atoms will tend to approach orthogonal to and remain on the sides, rather than funnel down to the base. This has been observed in molecular dynamics studies.⁵⁶ However, we have previously emphasized that these configurations are statistically insignificant for low- T growth.^{32,35} Even for higher T , where the formation of mounds or "pyramids" occurs, the sides typically have much smaller slopes than (111) facets, and the funneling component of the deposition dynamics corresponds to incoming atoms deflecting from *step edges* on a locally (100) surface. We note, however, that there may be other "transient dynamics" processes associated with deposition, not included in the funneling model,³² and which can affect film morphology (see section VI).

V. Transition to Multilayer Growth: Kinematic Diffraction Theory

Below we develop a *kinematic* or *single-scattering* theory^{5,57} appropriate for diffraction from the general film morphologies described in section IV. We use notation appropriate to a simple-cubic geometry to avoid added complications which arise for an fcc or bcc geometry (cf. section IV and ref 49). This theory should accurately describe diffraction profiles obtained from low energy electron diffraction (LEED). However, it might be less precise for reflection high energy electron diffraction (RHEED) due to dynamic scattering and also since the electron beam might be shadowed from parts of the mounded surface due to its small incident angle. The theory also does not reflect the strong step sensitivity of atom beam scattering.

For *lateral* momentum transfer, \mathbf{q} , and *vertical* momentum transfer, q_\perp (in units where the width of the Brillouin zone is 2π), the total kinematic diffracted intensity is given by the Fourier transform^{5,57}

$$I(\mathbf{q}, q_\perp) = \sum_{\delta \mathbf{l}} \exp[i\mathbf{q} \cdot \delta \mathbf{l}] C(q_\perp, \delta \mathbf{l}) \quad (16)$$

where

$$C(q_\perp, \delta \mathbf{l}) = \sum_n \exp[iq_\perp n] G_n(\delta \mathbf{l}) \quad (17)$$

Then the kinematic intensity is naturally decomposed into *Bragg delta-function* and *diffuse* components as

$$I_{\text{Bragg}}(\mathbf{q}, q_\perp) = (2\pi)^2 A_{\text{Bragg}}(q_\perp) \sum_{n,m} \delta[\mathbf{q} - 2\pi(n, m)] + I_{\text{diff}}(\mathbf{q}, q_\perp) \quad (18)$$

Using $G_{n \geq 0}(\infty) = \sum_{j \geq 0} P_j P_{n+j}$, from section IV, one obtains

$$A_{\text{Bragg}}(q_\perp) = C(q_\perp, \infty) = \left| \sum_{j \geq 0} \exp[iq_\perp j] P_j \right|^2 \quad (19)$$

and setting $\Delta C(q_\perp, \delta \mathbf{l}) = C(q_\perp, \delta \mathbf{l}) - C(q_\perp, \infty)$, one obtains

$$I_{\text{diff}}(\mathbf{q}, q_\perp) = \sum_{\delta \mathbf{l}} \exp[i\mathbf{q} \cdot \delta \mathbf{l}] \Delta C(q_\perp, \delta \mathbf{l}) \quad (20)$$

V.1. Submonolayer or Layer-by-Layer Growth.

Here we consider submonolayer growth with no second layer population, or strict layer-by-layer growth, and set $\theta = k + \delta\theta$ with integer k ($=0$ for submonolayer growth). One has the exact relations

$$A_{\text{Bragg}}(q_\perp) = 1 - 2[1 - \cos(q_\perp)](1 - \delta\theta)\delta\theta = 1 - 2[1 - \cos(q_\perp)]W^2 \quad (21)$$

so the antiphase Bragg intensity satisfies $A_{\text{Bragg}}(\pi) = (1 - 2\delta\theta)^2$. It also follows exactly that

$$\Delta C(q_\perp, \delta \mathbf{l}) = [H(\infty) - H(\delta \mathbf{l})][1 - \cos(q_\perp)] \quad (22)$$

so $I_{\text{diff}}(\mathbf{q}, q_\perp)$ is obtained essentially by direct Fourier transform of $H(\delta \mathbf{l})$. The previously mentioned overshoot or "weak oscillation" in $H(\delta \mathbf{l})$, results in a negative minimum in ΔC , which produces a "Henzler ring" feature⁵⁸ in $I_{\text{diff}}(\mathbf{q}, q_\perp)$ with the diameter of the ring, d , roughly proportional^{3,11,46} to $1/l_{av}$ (see Figure 5b).

V.2. Rough Multilayer Growth. Using the general representation (13) for the height distribution P_j , one can

(55) Weeks, J. D.; Gilmer, G. H.; Jackson, K. A. *J. Chem. Phys.* **1976**, 65, 712.

(56) Halstead, D.; DePristo, A. E. *Surf. Sci.* **1993**, 286, 275.

(57) Wollschläger, J.; Falta, J.; Henzler, M. *Appl. Phys. A* **1990**, 50, 57.

(58) Hahn, P.; Clabes, J.; Henzler, M. *J. Appl. Phys.* **1980**, 51, 2079.

apply the Poisson summation formula⁵⁹ to evaluate the dominant contribution to the antiphase Bragg intensity $A_{\text{Bragg}}(\pi)$. One obtains $A_{\text{Bragg}}(\pi) \approx 4\text{Re}\{e^{-i\pi\theta} f(\pi W)\}$ for large enough W that one can ignore higher order terms in the Poisson summation formula (but W must also be small compared with the Poisson growth value of $\theta^{1/2}$). Further, invoking the cumulant expansion for f yields³¹

$$A_{\text{Bragg}}(\pi) \approx 4 \cos^2[\pi\theta - \kappa_3\pi^3 W^3/3! + \dots] \exp[-\pi^2 W^2 + 2\kappa_4\pi^4 W^4/4! - \dots] \quad (23)$$

This provides the first correct characterization of the oscillatory decay of $A_{\text{Bragg}}(\pi)$. A detailed derivation of this result will be presented elsewhere.⁶⁰ While it might be, at least implicitly, assumed that the height distributions, f , are Gaussian (at least in self-affine growth models), leading to the simple form $A_{\text{Bragg}}(\pi) \approx 4 \cos^2(\pi\theta) \exp(-\pi^2 W^2)$, we find significant deviations for unstable growth models. In particular, an observed negative skewness, $\kappa_3 < 0$, leads to a shift in the zeros of $A_{\text{Bragg}}(\pi)$ below half-monolayer coverages.³¹ See parts b and d of Figure 6.

Similarly, using the representation (14) for G_m together with the Poisson summation formula, yields

$$C(q_{\perp}, \delta l) \approx \hat{g}[[q_{\perp}]H(\delta l)^{1/2}] \quad (24)$$

where $\hat{g}(k) = \int dx e^{ikx} g(x) \rightarrow 0$, as $k \rightarrow \pm\infty$, and $[q_{\perp}]$ means “ q_{\perp} modulo 2π ”, with $-\pi \ll [q_{\perp}] \ll \pi$. At the out-of-phase condition, $[q_{\perp}] \approx \pm\pi$, there is an extra factor of 2 on the right hand side of (24). For large W , where $C(q_{\perp}, \infty)$ is negligible, one naturally implements the approximation

$$I_{\text{diff}}(\mathbf{q}, q_{\perp}) \approx \sum_{\delta l < \xi} \exp[i\mathbf{q} \cdot \delta l] \hat{g}[[q_{\perp}]H(\delta l)^{1/2}] \quad (25)$$

It is clear that if $H(\delta l)$ adopts a stationary form for fixed δl , then I_{diff} will also adopt a stationary form. Furthermore, I_{diff} will be independent of the details of the evolving form of $H(\delta l)$ for “large” δl , where $H = O(W^2)$, and the \hat{g} factor in (25) is small. Finally, if H increases slowly over a broad range of δl (as is expected for large submonolayer l_{av}), and if $H(\delta l) \approx H(\delta l)$ is roughly rotationally invariant, then one naturally writes

$$I_{\text{diff}}(\mathbf{q}, q_{\perp}) \approx 2\pi \int_0^{\xi} dr r J_0(qr) \hat{g}[[q_{\perp}]H(r)^{1/2}] \quad (26)$$

We now discuss the form of I_{diff} for the two growth paradigms:

(A) Self-Affine Growth Models. Assuming a Gaussian form for G_n (or g), one obtains $C(q_{\perp}, \delta l) \approx \exp\{-[q_{\perp}]^2 H(\delta l)/2\}$ from (24). Then invoking the form (15) for $H(\delta l)$ (assuming that $l_0 \ll \eta$), and substituting into (26), leads directly to the key result of Yang *et al.*⁵

$$I_{\text{diff}}(\mathbf{q}, q_{\perp}) \approx (\eta[q_{\perp}]^{-1/\alpha})^2 \int_0^{\infty} dy y \exp(-y^{2\alpha}) J_0(q\eta[q_{\perp}]^{-1/\alpha} y) \quad (27)$$

This profile exhibits no ring structure or “splitting” (see Figure 5d). Clearly, the full-width-at-half-maximum (fwhm) is inversely proportional to the time-invariant constant η . If $\eta \sim l_{\text{av}}$, then one could say that the submonolayer structure selects the width of the subsequent time-invariant diffraction profile (cf. ref 61).

(59) Courant, R.; Hilbert, D. *Methods in Mathematical Physics* Interscience: New York, 1953; Vol. 1.

(60) Evans, J. W.; Bartelt, M. C.; Thiel, P. A. To be submitted to *Surf. Sci. Rep.*

(61) Ernst, H.-J.; Fabre, F.; Folkerts, R.; Lapujoulade, J. *Phys. Rev. Lett.* **1994**, *72*, 112.

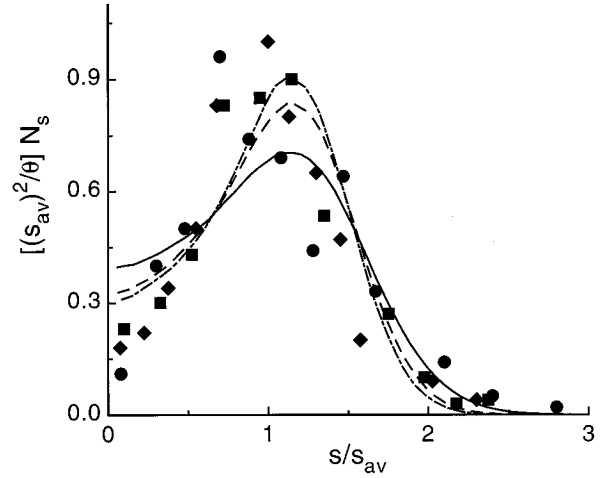


Figure 8. Scaled island size distributions, $[(s_{\text{av}})^2/\theta] N_s$, versus s/s_{av} . Symbols are Fe/Fe(100) STM data⁶² at 295 K (●), 383 K (■), and 407 K (◆), for $\theta \approx 0.07$ ML and $R \approx 0.7$ ML/min. Solid lines are $i = 1$ simulation results²⁴ at 295 K, with $E_d = 0.45$ eV and $\nu = 10^{12}$ /s. Solid lines indicate no cluster mobility. Dashed lines include dimer mobility with a barrier of 0.55 eV. Dot-dashed lines include dimer and trimer mobility with an equal barrier of 0.55 eV.

(B) Unstable Growth Due to a Step-Edge Barrier.

Here our studies suggest that the standard assumption of Gaussian height-difference distributions is not justified. On the other hand, for a range of shorter separations, g may be reasonably approximated with a rational function. Now (24) becomes³¹

$$C(q_{\perp}, \delta l) \approx \exp\{-|\text{Im}\lambda[q_{\perp}]H(\delta l)^{1/2}\} \quad (28)$$

where λ is the pole of g closest to the real axis (see refs 31 and 60 for details). This form can be used in (25) or (26) to obtain a suitable expression for I_{diff} .

It is clear from (28) that the enhanced “overshoot” region of $H(\delta l)$ with increasing θ has little influence on $C(q_{\perp}, \delta l)$ since it is in the “exponential tail”. Consequently, just as for (A), the splitting in the profile disappears (Figure 5f). For very well-developed mounds with slope S , where $H \sim [(\delta l)S]^2$, the fwhm of I_{diff} must be proportional to S .

VI. Analysis of Metal(100) Homoepitaxy for Specific Systems

Here we consider just two systems, but the basic features described should apply in general to metal(100) homoepitaxy.

VI.1. Homoepitaxy on Fe(100). Scanning Tunneling Microscopy (STM) studies⁶² have examined *submonolayer nucleation and growth* for T between 295 and 625 K, and $R \approx 0.7$ ML/min. The variation of the island density, $N_{\text{av}} \sim \exp[0.15 \text{ eV}/(k_B T)] \sim \exp[1/3 E_d/(k_B T)]$, for 295 K $< T < 525$ K, at a fixed coverage of $\theta = 0.07$ ML, implies that⁶² $E_d \approx 0.45$ eV if one assumes a critical size of $i = 1$ (at least for the lower portion of this T -range). The variation of N_{av} with R was not measured to determine if $\chi = 1/3$. Support for the claim that $i = 1$ comes only from comparison with an appropriate simulation model for irreversible nucleation and growth of square islands.¹¹ With the above E_d , this model matches the actual experimental values of N_{av} .

For a more detailed comparison, in Figure 8 we show the full island size distribution from these $i = 1$ square-

(62) Stroscio, J. A.; Pierce, D. T.; Dragoset, R. A. *Phys. Rev. Lett.* **1993**, *70*, 3615. Stroscio, J. A.; Pierce, D. T. *Phys. Rev. B* **1994**, *49*, 8522. *J. Vac. Technol. B* **1994**, *12*, 1783.

island simulations,¹¹ together with the experimental observations for $T \lesssim 400$ K. The agreement is fairly good, certainly compared with results from models with $i > 1$ (see refs 3, 12, and 15). However, the simulations predict higher densities of small islands than those observed and thus a slightly lower peak in the normalized scaling function. This discrepancy can be removed by incorporating some diffusion of small clusters,²⁷ which does not significantly affect N_{av} , but it could also be due to coarsening effects. Other simulation studies^{12,15} with $i = 1$ and *no* mobility of small clusters appeared to better fit the experimental data, but we believe that this was an artifact of the fractal structure of islands incorporated in these models [which is inappropriate for Fe/Fe(100)].

The above STM studies⁶² also reveal a distinct variation of $N_{av} \sim \exp[0.5 \text{ eV}/(k_B T)] \sim \exp[(i+2)^{-1}(iE_d + E_i)/(k_B T)]$ with $T > 525$ K. Using a rate-equation analysis to match observed N_{av} values, we first identified this behavior³ as corresponding to a direct jump from $i = 1$ to $i = 3$ (cf. section III), with $E_{bond} \approx E_3/2 \approx 0.65$ eV. Using the criteria of section III, one obtains $T_{1+} \approx 460$ K, $T_{3-} \approx 585$ K, and $T_{3+} \approx 640$ K (using $\delta E_b(4) = 2E_{bond}$), consistent with the above observations. Since $\sigma = E_{bond}/E_d \approx 1.4$ is quite "large", there is a well-defined $i = 3$ regime. Simulations¹² have been performed for the shape of the island size distribution from a model of type B with significant single-bond breaking, but *excluding* double-bond breaking on a square lattice, and thus corresponding to $i = 3$. These agree well with the experimental results for $T \approx 575$ – 625 K. However, we also wish to emphasize the broad transition region from $i = 1$ to $i = 3$: $T_{3-} - T_{1+} \approx 125$ K. Ratsch *et al.*¹⁵ have shown that the shape of the size distribution changes continuously across this transition, and can be parameterized by \mathcal{R} . (Alternatively, Y could be used.)

Contrasting the above analysis, Feibelman⁶³ suggests that E_{bond} should be much smaller. To reproduce the high- T Arrhenius behavior of N_{av} , he then proposes a crossover from a dominant exchange diffusion mechanism with $E_d = 0.45$ eV at low T , to another mechanism with much larger $E_d \approx 0.8$ eV, say, at higher T (so then $E_{bond} \approx 25$ meV). Note that this also requires the prefactor for the high- T mechanism to be at least three orders of magnitude larger than for the low- T mechanism. Also, lowering E_{bond} dramatically reduces the extent of the $i = 1$ regime, which becomes apparently inconsistent with experimental observations.

Next we analyze *multilayer growth and kinetic roughening* for Fe/Fe(100) at $T = 295$ K where island formation is irreversible. Here STM images reveal that the film roughens quickly.⁵⁴ Analysis of the layer coverage distributions⁵⁴ shows that $\beta \approx 0.15$ – 0.18 . Parallel RHEED studies⁵⁴ revealed a consistent strong damping of the (0,0)-beam intensity oscillations, and a transition from initially strongly split diffraction profiles, to profiles where the splitting has almost disappeared by ~ 100 ML. Independent high-resolution (HR) LEED studies⁶⁴ of growth estimated that $\beta \approx 0.22$ and $\alpha \approx 0.79$ based on (27), although one might expect that $\alpha = 1$ due to mounding. Nonsplit profiles were always observed in contrast to RHEED (but the lack of initial splitting was a consequence of starting from an imperfect "substrate").

To model this behavior, we extended our simulations of submonolayer nucleation and growth of square islands with $i = 1$ to the multilayer regime. We used the correct 4-fold-hollow (4FH) adsorption site geometry, and incor-

Table 2. Comparison of Simulation [SIM] Results for the Root Mean Square Interface Width, W (in Vertical Lattice Units), with Experiment [EXP], up to 20.5 ML, for Different Choices of the Step-Edge Barrier, E_{Sch} ^a

θ (ML)	$W^{[EXP]}$	$W^{[SIM]} < W^{[EXP]}$ ($E_{Sch} = 40$ meV)	$W^{[SIM]} \approx W^{[EXP]}$ ($E_{Sch} = 45$ meV)	$W^{[SIM]} > W^{[EXP]}$ ($E_{Sch} = 50$ meV)
0.8	0.509	0.491	0.508	0.520
1.8	0.598	0.583	0.612	0.640
2.9	0.801	0.656	0.688	0.728
5.3	0.850	0.771	0.812	0.856
10.0	0.952	0.905	0.962	1.019
20.5	1.053	0.975	1.049	1.083

^a The simulations used the Fe/Fe(100) parameters: $E_d = 0.45$ eV, $\nu = 10^{12}$ /s, $T = 20$ °C, and $R = 0.7$ ML/min. These choices match the observed⁶² mean island density, $N_{av} \approx 3 \times 10^{-3}$ /site, at 0.07 ML.

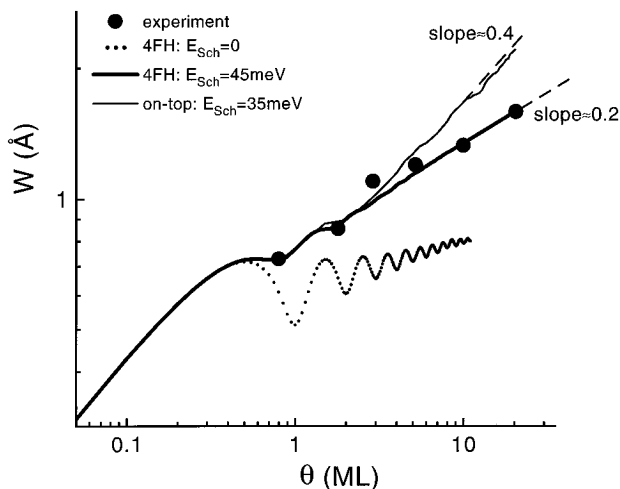


Figure 9. Variation of W with $\theta \lesssim 20$ ML, at 20 °C, for $R \approx 0.7$ ML/min. Circles are experimental data⁶² for Fe/Fe(100). Simulation results using $E_d = 0.45$ eV and $\nu = 10^{12}$ /s, with $E_{Sch} = 45$ meV (thick solid line) and $E_{Sch} = 0$ (dotted line), using a 4FH adsorption site geometry. We also show simulation results for an on-top adsorption site geometry with $E_{Sch} = 35$ meV (thin solid line), which fits the experimental data (only) up to ~ 5 ML.

porated realistic downward funneling or deflection dynamics. (Atoms deposited at step edges and on microprotrusions are funneled down to lower 4FH sites.) The only additional model parameter is an *effective* Schwoebel barrier, E_{Sch} , for downward transport of diffusing adatoms that reach step edges. (Note that we take the same E_{Sch} for all island edge sites.) Choosing $E_d = 0.45$ eV to match the submonolayer island density, as above, we then vary E_{Sch} to obtain the best match to the experimental⁵⁴ θ_j (and thus to W), at various coverages below about 5 ML. This yields $E_{Sch} \approx 0.045 \pm 0.005$ eV (see Table 2 and Figure 9). This choice produces kinetic roughening with an effective $\beta \approx 0.2$ (for $5 \text{ ML} < \theta < 30 \text{ ML}$, see Figure 10), which reasonably matches the experimental value. Similar results have been obtained by Amar and Family.⁶⁵ A much more detailed presentation of our simulation results for film morphology will be published elsewhere. We have also performed an analysis of the temperature dependence of roughening which is entirely consistent with the general scenario described in section IV.

We emphasize that precise treatment of adsorption site geometry and downward funneling deposition dynamics is crucial here in fitting the experiment. Use of a simple-cubic geometry allows reasonable estimation of E_{Sch} and prediction of behavior for $\theta < 5$ ML but produces much greater subsequent roughening than seen in experiment.

(63) Feibelman, P. *Phys. Rev. B* **1995**, 52, 12447.

(64) He, Y.-L.; Yang, H.-N.; Lu, T.-M.; Wang, G.-C. *Phys. Rev. Lett.* **1992**, 69, 3770.

(65) Amar, J. G.; Family, F. *Phys. Rev. B* **1995**, 52, 13801 and private communication.

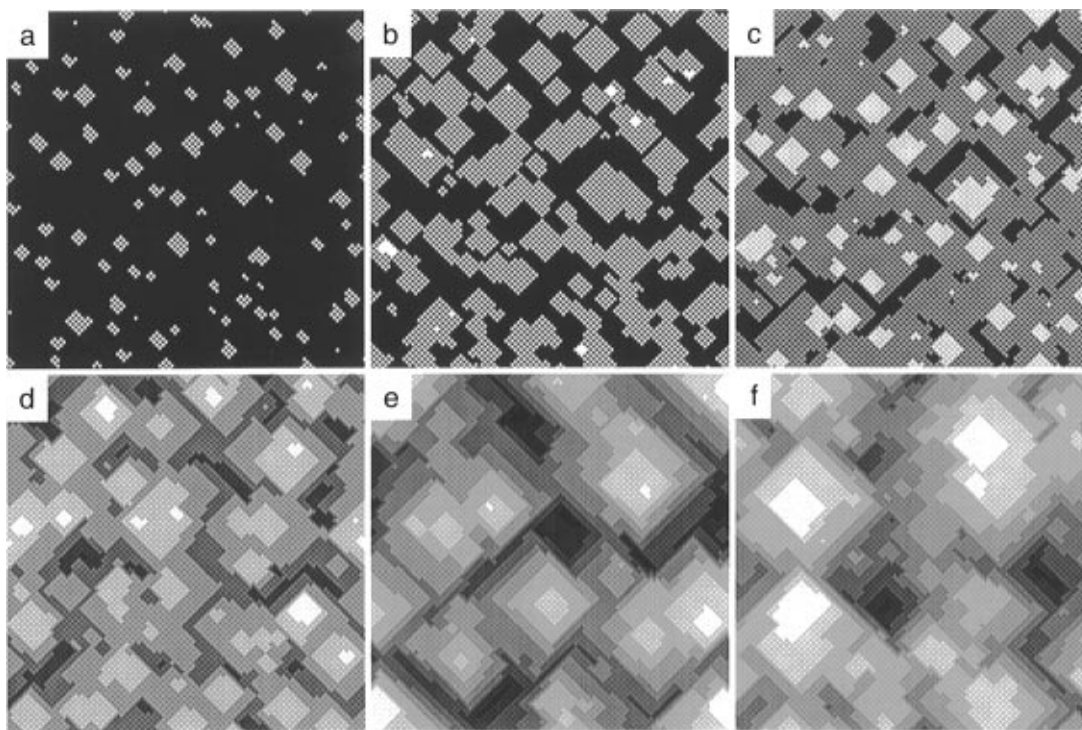


Figure 10. Adlayer morphologies from simulations using $E_d = 0.45$ eV, $E_{\text{Sch}} = 45$ meV, $\nu = 10^{12}$ /s, $T = 295$ K, and $R \approx 0.7$ ML/min. Darker regions correspond to lower levels. Total coverages (in ML) from (a–f) are 0.1, 0.5, 1, 5, 50, and 100.

See Figure 9. The same is true even if one mimics downward funneling in the simple-cubic geometry, e.g., by allowing 50% of atoms depositing on top of sites at the straight edges of islands to “deflect” down.

VI.2. Homoepitaxy on Cu(100). Submonolayer nucleation and growth has been studied in this system primarily via surface-sensitive diffraction techniques.^{66–69} A ring structure is invariably observed in the “split” diffraction profile. The ring diameter, d^* , is typically assumed to be inversely proportional to the mean island separation, i.e., $d^* \propto 1/l_{\text{av}} = N_{\text{av}}^{1/2} \sim (h/R)^{1/2}$. However, interpretation of observed behavior has been controversial.^{3,41,66,67,70}

He-beam scattering studies⁶⁶ found that $d^* \sim R^{0.27}$ for $T = 220$ K, and $d^* \sim R^{0.23}$ for $T = 230$ K, with $1/2000$ ML/s $< R < 1/100$ ML/s, at fixed $\theta = 0.5$ ML. They also found that $d^* \sim \exp[0.07 \text{ eV}/(k_B T)]$ for $170 \text{ K} < T < 250 \text{ K}$ with $R \approx 1/1270$ ML/s. This suggests^{66,67} that $\chi_{\text{eff}} \approx 1/2$, so $i = 2$ from (1), so $2E_d + E_2 \approx 8 \times 0.07 \text{ eV}$ from the Arrhenius behavior of d^* . However, one then obtains a rather low $E_d < 0.2 \text{ eV}$, for reasonable $E_2 = E_{\text{bond}} \approx 0.2 \text{ eV}$. Ernst *et al.*^{66,67} instead argue that d^* is most sensitive to the largest islands, whose separation satisfies a different “transient” scaling, and extract E_d accordingly. However, simulations do not support their claim.^{3,11} The situation was clarified by recent HRLEED studies⁶⁸ of flux scaling at 223 K which do in fact show that χ_{eff} crosses over from $\sim 1/2$ to an asymptotic value of $\sim 1/3$ at sufficiently low fluxes ($R < 1/1000$ ML/s). This provides convincing evidence that $i = 1$ here.

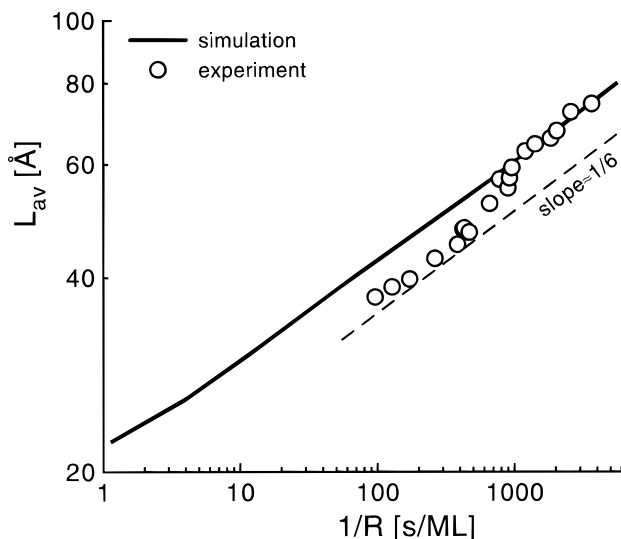


Figure 11. Characteristic real-space length, $L_{\text{av}} = 4\pi/d^*$, obtained from the ring diameter, d^* , of the diffraction profile, versus the inverse flux, $1/R$, at 0.3 ML. Open circles are experimental data⁶⁸ for Cu/Cu(100) at 223 K. Solid line are $i = 1$ square-island simulation data with $h = 450$ /s.

On the basis of this observation, we have simply matched the ring diameter behavior, $d^* \approx 4.6(R/h)^{1/6}$, obtained from our square-island simulations with $i = 1$, to the HRLEED behavior, $d^* \approx 1.66R^{0.17}$, for asymptotically small R , at fixed $\theta = 0.3$ ML. See Figure 11. This yields $h \approx 450$ /s at 223 K, so in fact $E_d \approx 0.40 \text{ eV}$, assuming that $\nu \approx 5 \times 10^{11}$ /s.

The origin of the “anomalous” $\sim R^{1/4}$ behavior of d^* for $R > 1/1000$ ML/s, duplicated by HRLEED⁶⁸ and He-beam scattering^{66,67} studies at fixed $\theta = 0.3$ – 0.5 ML and $T \approx 220$ K, has been examined in recent simulations by Breeman *et al.*⁷¹ tailored to this system. Their results indicate that the key ingredient is the *restructuring of islands upon coalescence*. Described below is an analysis that we have performed to test and elucidate this idea.

(66) Ernst, H.-J.; Fabre, F.; Lapujoulade, J. *Phys. Rev. B* **1992**, *46*, 1929.

(67) Ernst, H.-J.; Fabre, F.; Folkerts, R.; Lapujoulade, J. *J. Vac. Sci. Technol. A* **1994**, *12*, 1809.

(68) Zuo, J.-K.; Wendelken, J. F.; Dürr, H.; Liu, C.-L. *Phys. Rev. Lett.* **1994**, *72*, 3064.

(69) Dürr, H.; Wendelken, J. F.; Zuo, J.-K. *Surf. Sci.* **1995**, *328*, L527.

(70) Zangwill, A. In *Evolution of Surface and Thin Film Microstructure*; Atwater, H. A.; Chason, E.; Grabow, M.; Lagally, M. Eds.; MRS Proceedings; Materials Research Society: Pittsburgh, PA, 1993; Vol. 280, p 121.

Our above mentioned square-island simulations yielding $d^* \sim R^{1/6}$, at fixed θ , were performed with *no restructuring* (NR) of islands upon coalescence. Modifying the simulations to allow *complete restructuring* (R) to form larger squares produces the *same* scaling. Furthermore, we find that $d^*(R)/d^*(NR) \approx 1$ for θ below about 0.3 ML (due to limited coalescence). However, $d^*(R)/d^*(NR)$ decreases below unity for higher θ , since the onset of significant restructuring increases the correlation length of the adlayer, thus reducing d^* . This suggests⁷¹ the following scenario for the observed variation of d^* with R . For *large* R , there is insufficient time for restructuring following coalescence of islands, and thus $d^*(\text{exp}) \sim d^*(NR) \sim A_{NR}R^{1/6}$. For *low* R , significant restructuring is possible, and thus $d^*(\text{exp}) \sim d^*(R) \sim A_R R^{1/6}$ with $A_R > A_{NR}$. The anomalous scaling reflects a *crossover* between these two regimes.⁷²

The above HRLEED study⁴³ also showed a distinct flux scaling, $d^* \sim R^{0.3}$ or $\chi \approx 3/5$, in the range $1/4000 < R < 1/1000$ ML/s, at the higher temperature of 263 K. One might naturally identify this as a transition from $i = 1$ at 220 K, to $i = 3$ at 263 K (cf. section III). We believe that this behavior is best fit choosing E_{bond} around 0.2 eV, so then $T_{1+} \approx 215$ K, $T_{3-} \approx 270$ K, and $T_{3+} \approx 280$ K (using $E_d = 0.4$ eV, $\delta E_b(4) = 2E_{\text{bond}}$, and $R = 0.001$ ML/s). Then $\sigma \approx 0.5$ is “small”, so no extended regime of $i = 3$ exists. χ should vary strongly with T , so the observation of a classic $i = 3$ value at 263 K is somewhat accidental!

An HRLEED study of the Arrhenius behavior of d^* for T between 180 and 260 K, for $R = 3.21 \times 10^{-4}$ ML/s, revealed an apparent sharp break in slope from 0.06 eV, for $T < 225$ K, to 0.12 eV, for $T > 225$ K. Assuming that the region of $T < 225$ K corresponds to $i = 1$, as supported by the flux scaling results, yields the estimate $E_d = 0.36 \pm 0.03$ eV, consistent with our simulation result above. In ref 69, the data above 223 K were fit to a clean $i = 3$ regime⁶⁹, producing an unreasonably low estimate for $E_{\text{bond}} \approx 0.06$ eV. We find⁷² that the observed behavior corresponds instead to a gradual crossover from $i = 1$ to $i = 3$, with $E_{\text{bond}} \approx 0.2$ eV (cf. ref 16).

The *multilayer growth and kinetic roughening* of Cu/Cu(100) is also rather complicated. He-beam scattering studies^{61,67} reveal a transition from “smooth growth” for $T \geq 250$ K, to rough growth for $T \approx 200$ K with $\beta \approx 1/2$, to smoother “reentrant” growth for $T \approx 160$ K with $\beta \approx 0.26$ (and possibly smoother growth for lower T). Large- \mathbf{q} features of the diffraction profile indicated the development of “pyramids” or mounds with sides corresponding to (113) facets at 160 K, and (115) facets at 200 K. It was also found that $\alpha \approx 1$ at both 200 K and 160 K, consistent with mounds of selected slope.²⁶ Finally, a transition was observed⁶⁷ during film growth from a split diffraction profile to the nonsplit form, expected for rough films (cf.

section V). The final saturation width of the profile appeared to correlate with the submonolayer characteristic length.⁶⁷

Rough growth with $\beta \approx 1/2$ at 200 K has been explained⁶⁷ by the presence of a “large” Schwoebel barrier, E_{Sch} . This barrier is insurmountable prohibiting downward thermal transport at $T = 200$ K and below, but not at $T \geq 250$ K. To explain the smoother growth at 160 K, it has been suggested⁶⁷ either that E_{Sch} is lowered or becomes less effective due to the smaller size or perhaps “frizzier” edges of islands. Instead, as in section IV, we propose that smoother growth is a natural consequence of enhanced nonthermal downward funneling from step edges. The concentration of edges increases as the islands become smaller for decreasing T , and eventually the adlayer becomes a quasi-random distribution of adatoms. The decrease in β is consistent with such a model since, based on studies of the downward funneling model,⁵¹ one should expect that $\beta \rightarrow 0$, as $T \rightarrow 0$.

However, the “anomalously” large lateral correlation lengths observed³³ in this system for submonolayer coverages at very low T are not consistent with the standard downward funneling model⁴⁹ (they appear narrower than those predicted by the model). We previously disputed the claim³³ that this behavior is due to “transient mobility” between 4FH adsorption sites.^{32,51} Instead, we are exploring a modified model involving nonthermal short-range motion or “clumping” of atoms deposited nearby existing adatoms. This feature produces an increase in the correlation length and thus narrowing of the profiles, as required, but could also potentially modify the roughening behavior. Details of this analysis will be reported elsewhere.

VI. Conclusions

We have examined realistic models for submonolayer nucleation and growth in metal(100) homoepitaxy, and subsequent multilayer growth. Some basic issues regarding the scaling of submonolayer island density, and transitions in critical size, are discussed. Fundamental and generic features of the real-space morphology of roughening multilayer films are identified, and an appropriate reciprocal-space kinematic diffraction theory is developed. These models and results are applied to provide a detailed understanding of observed behavior during Fe(100) and Cu(100) homoepitaxy.

Acknowledgment. This work was supported by NSF Grant No. CHE-9317660 and IPRT (ISU). It was performed at Ames Laboratory which is operated for the US Department of Energy by Iowa State University under Contract No. W-7405-Eng-82. We gratefully thank J. A. Stroscio and D. T. Pierce for providing unpublished data for Fe/Fe(100).

LA940698S

(71) Breeman, M. Private communication, and presentation at the WE-Heraeus Seminar 140 on “Fundamental Processes in Epitaxy” (Bad Honnef, February 1995).

(72) Bartelt, M. C.; Evans, J. W.; *Surf. Sci. Comment*, submitted.